Physics – Uspekhi **57** (4) 317 – 341 (2014)

100th ANNIVERSARY OF THE BIRTH OF Ya B ZELDOVICH

PACS numbers: 97.60.Lf, **98.65.–r**, 98.80.Bp

Clusters of galaxies

A A Vikhlinin, A V Kravtsov, M L Markevich, R A Sunyaev, E M Churazov

DOI: 10.3367/UFNe.0184.201404a.0339

Contents

1. Introduction 317
2. Modeling the formation of the large-scale structure and galaxy clusters 318
2.1 Large-scale structure of the Universe and the Harrison–Zeldovich spectrum of primordial perturbations; 2.2 Numerical simulations of structure formation; 2.3 Galaxy clusters in the cosmic web of hot intergalactic gas; 2.4 Modeling the galaxy cluster mass function; 2.5 Measuring the total masses of clusters and their mass function
3. Cosmological studies with galaxy clusters 324
3.1 Galaxy cluster catalogs with high statistical 'purity'; 3.2 Detailed measurements of individual object parameters; 3.3 Cluster mass measurements; 3.4 Geometrical test using X-ray data and the Sunyaev–Zeldovich effect; 3.5 Geometrical test using the hot gas specific mass fraction $f_{\rm gas}$; 3.6 Measuring the large-scale structure growth rate; 3.7 Expected results of future experiments
4. Shocks in the intergalactic gas 328
4.1 Bullet cluster and dark matter properties; 4.2 Electron–proton temperature equilibration in hot plasma; 4.3 Constraints on diffusion in plasma; 4.4 Ultrarelativistic electrons in the intergalactic plasma; 4.5 Nearest prospects of cluster shock studies
5. Supermassive black holes in cluster centers 334
5.1 General picture; 5.2 Gas cooling; 5.3 Observational appearances of the interaction of gas and a supermassive black hole; 5.4 Mechanical energy dissipation; 5.5 Feedback mechanism; 5.6 Relation to the evolution of elliptical galaxies
6. Conclusion 339
References 339

Abstract. Galaxy clusters are formed via nonlinear growth of primordial density fluctuations and are the most massive gravitationally bound objects in the present Universe. Their number density at different epochs and their properties depend strongly on the properties of dark matter and dark energy, making clusters a powerful tool for observational cosmology. Observations of the hot gas filling the gravitational potential well of a cluster allows studying gasdynamic and plasma effects and the effect of supermassive black holes on the heating and cooling of gas on cluster scales. The work of Yakov Borisovich Zeldovich has had a profound impact on virtually all cosmological and astrophysical studies of galaxy clusters, introducing concepts such as the Harrison–Zeldovich spectrum, the Zeldovich approximation, baryon acoustic peaks, and the Sunyaev–Zeldovich effect. Here, we review the most basic properties of clusters and their role in modern astrophysics and cosmology.

A A Vikhlinin Space Research Institute, Russian Academy of Sciences, ul. Profsoyuznaya 84/32, 117997 Moscow, Russian Federation
E-mail: vikhlinin@iki.rssi.ru
Center for Astrophysics, 60 Garden St, Cambridge, MA 02138 USA
A V Kravtsov The University of Chicago, 5640 South Ellis Ave., Chicago IL 60637, USA
M L Markevich NASA Goddard Space Flight Center, Greenbelt, MD 20771, USA
R A Sunyaev, E M Churazov Space Research Institute, Russian Academy of Sciences, ul. Profsoyuznaya 84/32, 117997 Moscow, Russian Federation
E-mail: churazov@iki.rssi.ru
Max Planck Institute for Astrophysics, Karl-Schwarzschild-Str. 1, Postfach 1317, D-85741 Garching, Germany

Received 19 February 2014
Uspekhi Fizicheskikh Nauk **184** (4) 339 – 366 (2014)
DOI: 10.3367/UFNr.0184.201404a.0339
Translated by K A Postnov; edited by A M Semikhatov

1. Introduction

Galaxy clusters hold a special place in modern astrophysics and cosmology. Like all objects in the Universe, clusters were formed from tiny fluctuations generated during the Universe's inflationary expansion. We observe these perturbations as temperature fluctuations of the cosmic microwave background (CMB), which occurred when the age of the Universe was about 400,000 years. Linear perturbations on all scales grow at the same rate, and the formation time of a nonlinear object is fully determined by the initial perturbation amplitude. For a perturbation spectrum close to the Harrison–Zeldovich spectrum, the amplitude decreases with increasing the size (mass) of the object, and more massive objects are formed at later times. In our Universe, galaxy clusters are the most massive objects (with a mass of about $10^{15}\,M_{\odot}$) that have managed to form to date. In a universe with a cosmological constant (dark energy), accelerated expansion slows down the perturbation growth rate, and clusters remain the most massive objects. This is why clusters are distinct among all other objects and can be used as a tool for measuring dark energy and neutrino properties.

Due to the huge mass of clusters, gravity dominates over all other processes, and clusters can be considered a representative piece of the Universe, in which the mass ratio of dark matter to baryonic matter is universal. Additionally, the huge mass of clusters causes gravitational lensing of more distant objects, which allows searching for objects enhanced by the gravitational lens effect at record high redshifts.

The gravitational well of a cluster is so deep that infalling gas is heated to temperatures of the order of 10 to 100 million Kelvin, which makes the clusters powerful sources of X-ray emission. At the same time, scattering of CMB photons on hot electrons leads to CMB spectral distortions (the Sunyaev–Zeldovich effect) and allows detecting clusters at any redshift. X-ray studies coupled with microwave observations render clusters a powerful tool of observational cosmology.

Galaxy clusters are dynamical objects that continue growing at the present time by swallowing less massive clusters. The comparison of gas and gravitating mass distributions sets nontrivial limits on the dark matter particle interaction cross sections. Cluster merging results in shocks and turbulent motion of gas. Radio and X-ray observations are used to study gasdynamic and plasma effects in a hot gas, including cosmic ray acceleration.

The time of radiative cooling of a hot gas in galaxy cluster centers is much less than the age of the Universe. Without an external energy source, the gas should cool, fragment, and form stars. But this is not so. The mechanical energy produced by the central supermassive black hole regulates the heat balance in the gas and prevents it from uncontrolled cooling. Generally, the interaction of the mechanical energy from the black hole with the gas is similar to processes occurring during powerful explosions in Earth's atmosphere. In a similar way, the supermassive black holes can affect the formation and evolution of galaxies at redshifts $z \sim 2-3$. Observations of nearby clusters allow detailed studies of this process.

Papers by Yakov Borisovich Zeldovich have had a profound impact on virtually all cosmological and astrophysical aspects of galaxy clusters. The Harrison–Zeldovich spectrum, the Zeldovich approximation, baryon acoustic oscillations, the Sunyaev–Zeldovich effect — all these topics are part of modern university courses and are currently actively used in theoretical, numerical, and observational astrophysics. The monograph by Zeldovich and Raizer, *Physics of Shocks Waves and High-Temperature Hydrodynamic Phenomena*, which gives a lucid description of the physics of hot gas, shock waves, and atmospheric explosions that determine observational appearances of the clusters, remains a handbook for astrophysicists. Currently, several dozen ground-based and space observatories are exploring galaxy clusters and effects predicted by Zeldovich. Under development are even more ambitious future projects, including Spectrum-Roentgen-Gamma (SRG), which should discover all massive clusters in the observed Universe.

In this review, we discuss the most general properties of clusters and their role in modern astrophysics and cosmology.

2. Modeling the formation of the large-scale structure and galaxy clusters

2.1 Large-scale structure of the Universe and the Harrison–Zeldovich spectrum of primordial perturbations

Although cosmological models usually assume a homogeneous and isotropic universe on large scales, significant

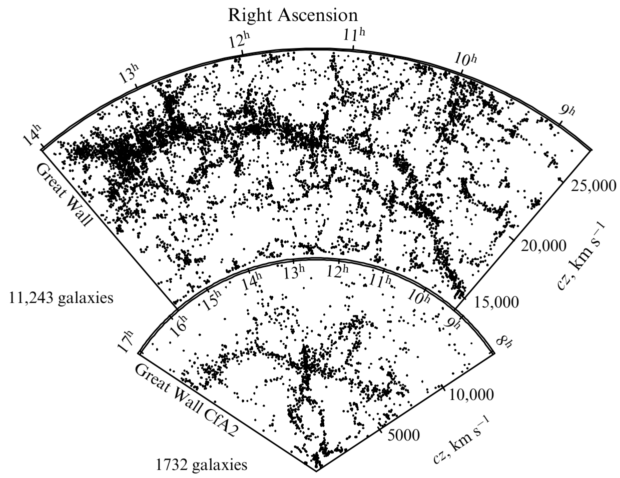

Figure 1. Large-scale structure in the distribution of galaxies in the CfA2 (Center for Astrophysics Redshift Survey) and SDSS (Sloan Digital Sky Survey) sky surveys [2]. The CfA2 volume (bottom cone) with a size of ≈ 200 Mpc shows filaments and voids around the Coma cluster (dense region in the center), including an almost horizontal filament called the 'Great Wall'. This galaxy distribution compellingly revealed the large-scale structure morphology, later named the 'Cosmic Web', and played an important role in developing structure formation models. The SDSS volume (upper segment) demonstrates the elongated filamentary structure, called the 'SDSS Great Wall' by analogy, which is three times as long as the CfA2 Great Wall.

inhomogeneities in galaxy distribution are observed on scales $\lesssim 100$ Mpc. The observed large-scale structure consists of groups and clusters of galaxies with a size of ~ 1 Mpc, connected by filaments and 'walls' with sizes up to ~ 100 Mpc. The filaments and walls are embedded in regions of a low galaxy density, called voids [1]. Figure 1 shows the observed large-scale structure [2].[1]

Models of the structure formation rely on several fundamental theoretical pillars. For example, primordial density perturbations, from which the observed structure originated, are assumed to be Gaussian (this assumption was recently confirmed with high accuracy by the results from the Planck satellite [3]). The statistical properties of the Gaussian density fluctuations are fully described by the power spectrum, which is equal to the ensemble-averaged square of the Fourier amplitudes of waves with a wave vector $\mathbf{k}$. The power spectrum $P(k)$, determined for the Fourier harmonics inside a sufficiently large spatial volume V, in the isotropic Universe depends only on the absolute value of the wave vector k:

$$P(k) \equiv \frac{1}{V} \left\langle |\delta_k|^2 \right\rangle . \tag{1}$$

The power spectrum, which has the dimension of volume, is frequently multiplied by k^3, which yields a dimensionless amplitude characterizing the typical density perturbation amplitude squared on a scale $\sim 1/k$:

$$\Delta^2(k) \equiv \frac{k^3}{2\pi^2} P(k) . \tag{2}$$

According to the modern paradigm of large-scale structure formation, these perturbations originated from quantum

[1] http://www.astrp.princeton.edu/universe/.

fluctuations on microscopic scales and grew to the cosmological scale during the primordial inflationary stage of the Universe's expansion (see, e.g., [4, 5]). Thus, inflationary models provide an elegant explanation of the origin of primordial perturbations: structures observed in the Universe on scales up to ~ 100 Mpc arose from quantum fluctuations of the inflationary field (or fields). These models also offer a natural explanation for both the Gaussian form of the perturbations and their assumed primordial spectrum.

Inflationary models [6–10] and predictions of the perturbation power spectrum [11–14] based on them appeared only in the early 1980s. But the general form of the primordial perturbation spectrum, $P(k) \propto k$, was advocated by Zeldovich in 1972, long before the first inflationary perturbation spectrum calculations [15].[2] Such a spectrum is said to be scale invariant, because it corresponds to the potential and metric fluctuation spectrum in which the typical fluctuation amplitude is independent of scale: $\Delta_{\phi}^2(k) \propto k^{-4}\Delta^2(k) \propto k^{-4}k^4 =$ const.

In paper [15] written in 1972, which rapidly became classical,[3] Zeldovich used simple physical arguments: he supposed that the Universe was originally in a cold state and was heated by the dissipation of small-scale metric perturbations through acoustic waves during the Universe's expansion, and these perturbations were found inside the cosmological horizon.

Thus, in Zeldovich's hypothesis, small-scale perturbations were postulated to be the source of the heating that is needed to explain the primordial nucleosynthesis and CMB. At the same time, on large scales, fluctuations must be large enough to explain the formation of observed galaxy clusters with masses from $\approx 10^{13}$ to $\approx 10^{15}\, M_{\odot}$. Zeldovich showed that the scale-invariant spectrum with a metric perturbation amplitude of the order of 10^{-4}, which did not contradict the CMB temperature perturbations at that time, can elegantly explain both cluster formation and sufficient heating of the early Universe.

Although the details of Zeldovich's arguments have not been confirmed by the later development of the standard cosmological model, many of his ideas anticipated cosmological model milestones. For example, the idea that the Universe began from a cold state and the subsequent reheating resulted in the creation of a huge number of particles and the baryon asymmetry is confirmed by inflationary models, in which the Universe becomes very cold during many cycles of exponential growth and requires reheating, in which high-temperature particles are created. The inflationary models also enabled the calculation of the expected metric perturbations spectrum, which turned out to be very close to a scale-invariant form [11–14] (see also the detailed review [5]). The metric perturbation amplitude, which is needed for the timely formation of the large-scale structure, according to Zeldovich's estimate turned out to be several orders of magnitude smaller than in the first inflationary models [13, 20], which stimulated the development of new, improved models.

During the last decade, observations of the CMB temperature fluctuations have shown that the primordial metric perturbation spectrum is indeed very close to the scale-invariant form. For example, recent papers devoted to the analysis of the Planck experiment data have demonstrated that the primordial perturbation spectrum has a power-law shape, $P(k) \propto k^{n_s}$, with $n_s = 0.9603 \pm 0.0073$ [21].

At the same time, the theoretical development of models of perturbation evolution in the baryon–photon plasma in the early Universe resulted in the creation of high-precision numerical methods (see, e.g., [22, 23]). These methods allow calculating the modification of the primordial scale-invariant spectrum due to different plasma processes (for example, suppression of perturbation growth during the radiation-dominated epoch and acoustic plasma oscillations decay). These precise model predictions and effects related to plasma processes are consistent, with ever growing accuracy, with a number of recent CMB observations [24, 25].

Measurements suggest that the ultimate perturbation spectrum $P(k)$ has the index changing from $n_s \approx 1$ on large scales (small values of k) to $n_s \sim -2$ on scales of the order of 100 Mpc and $n_s \sim -2.5$ on a scale of about 1 Mpc. As $k \to \infty$, the value of n_s tends to -3. The characteristic perturbation amplitude behaves as $\Delta^2(k) \propto k^3 P(k)$, and therefore increases with decreasing the spatial scale of perturbations to scales of the order of the Solar System size and less [26]. This increase leads to a hierarchical structure formation: first, structures appear on the smallest scales, and structures of larger scales arise later due to the merging of already formed structures.

2.2 Numerical simulations of structure formation

Structure formation at nonlinear stages is modeled by numerical calculations in which exact predictions of a linear perturbation spectrum are used to set the initial matter distribution. In numerical models, the initial conditions are set at already fairly late epochs (redshifts $50 \lesssim z \lesssim 200$). The evolution of perturbations before the initial time is calculated using a method proposed by Zeldovich in 1970 [27, 28]. The method is based on the well-known Lagrangian approach to the evolution of matter, which is widely used in hydrodynamics [29]. This approach turns out to be very successful for tracing the evolution of primordial cosmological density perturbations because typical inhomogeneities are quite 'oblate' [30]. The method of calculations proposed by Zeldovich, also known as the Zeldovich approximation, proved to be surprisingly exact for typical oblate perturbations (see, e.g., [31, 32]). In the limit case of the collapse of a one-dimensional plane wave, the Zeldovich method gives the exact solution, at least until the particle orbits intersect and caustics are formed.

Due to its accuracy and relative simplicity, the Zeldovich method was successfully applied for modeling structure formation in the 1970s, when direct numerical simulations of the structure were not yet possible [33–35]. For example, Figure 2 presents the result of two-dimensional calculations of the evolution of adiabatic perturbations with a power-law spectrum using the Zeldovich approximation [35]. These calculations demonstrated that the large-scale structure with characteristic filaments and voids, shown in Fig. 1, arises in a natural way from adiabatic Gaussian density perturbations (see also [36–38]).

During the following decades, the Zeldovich method served as the base for a number of analytic models of

[2] Arguments were also partially presented in the earlier paper [16]. The scale-invariant spectrum was also suggested in [17, 18] using totally different statistical arguments.

[3] The status of Zeldovich's work, as well as its impact, can already be clearly seen from the fact the scale-invariant spectrum has been called the Harrison–Zeldovich spectrum for many decades; this term is often used without referencing the original paper (see, e.g., [19]).

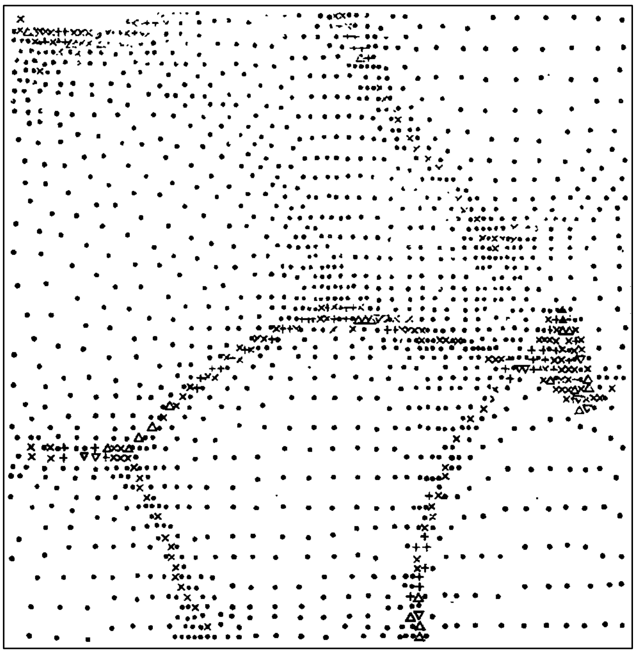

Figure 2. The result of two-dimensional calculations of the evolution of adiabatic perturbations with a power-law spectrum using the Zeldovich approximation [35], which shows that the large-scale structure with the characteristic filaments and voids (see Fig. 1) is naturally formed from the adiabatic Gaussian density perturbations.

structure formation [39–42] and numerical calculations of the nonlinear stage of the collapse of perturbations. In numerical simulations, this method became standard for setting initial conditions [33, 43–45], because it can be used for rather precise predictions of the evolution of the primordial perturbations until quite late times ($z \sim 50-100$), which allows skipping uninteresting numerical modeling of the early evolution in the quasilinear regime. Although the method of setting the initial conditions has recently been improved [46], it relies on the same Lagrangian approach used by Zeldovich, and the increase in accuracy has been achieved simply by accounting for second-order terms in the perturbation theory (in Zeldovich's original paper, only linear expansion terms were used).

At the same time, the fact that the Zeldovich approximation gives an exact solution in the one-dimensional collapse of a three-dimensional plane wave is widely used to test methods involved in simulations of the Universe's formation [43–50].

In numerical simulations, the equations of motion of matter are solved in the expanding coordinate frame, determined by the overall expansion of the Universe depending on cosmological parameters (in the standard model, the Hubble constant, the mean density of matter, and the dark energy density). However, the usual expansion is 'hidden' behind the specially chosen 'comoving' variables [33, 51, 52], such as the comoving coordinate $\mathbf{x}$ that is related to the physical coordinate $\mathbf{r}$ and the scale factor $a(t)$ as $\mathbf{x} = \mathbf{r}/a(t)$. The methods that are used in numerical simulations of structure formation include fast numerical algorithms for calculating gravity forces [53, 54] and, if the normal baryon–fermion material is modeled in addition to the collisionless dark matter, methods of numerical hydrodynamics [55].

Figure 3 shows the dark matter distribution in one of the modern numerical simulations of structure formation in the ΛCDM model (the model with the cosmological constant and cold dark matter). At early stages, numerous relatively small halos are formed, whose clustering is much stronger than the dark matter clustering [56, 57]. For example, in the left bottom corner in Fig. 3a, b, a high concentration of matter and halos in the form of a proto-cluster is visible. In Fig. 3d ($z = 0$), a cluster formed in this region can be seen. At late evolutionary stages (Fig. 3c, d), filaments and voids 100 Mpc in size are seen. At redshifts between $z = 1$ and $z = 0$, the large-scale structure does not change significantly, because at $z < 1$, the low matter density in this model and the cosmological constant lead to a high expansion rate, which stops the collapse of filaments. In the comoving reference frame used in Fig. 3, the large-scale structure is 'frozen' during such a rapid expansion. However, the evolution does not stop inside the forming massive cluster. Massive clusters continue rapid evolution at $z < 1$, which allows using them as one of the cosmological probes.

2.3 Galaxy clusters in the cosmic web of hot intergalactic gas

During collapse, baryonic gas follows the dark matter that dominates on large scales. Strong shocks and adiabatic compression raise the gas temperature to $\sim 10^5 - 10^7$ K in large-structure filaments and in the largest halos with masses of $\sim 10^{14} - 10^{15}\, M_{\odot}$, corresponding to the observed cluster masses [58]. Already in the 1970s, the models relying on the Zeldovich approximation showed that at late stages of the structure formation, most of the diffusive baryonic gas must be in the hot phase of filaments and galaxy clusters [35, 58], which was later confirmed by numerical calculations of hydrodynamics and thermodynamics of the collapsing gas

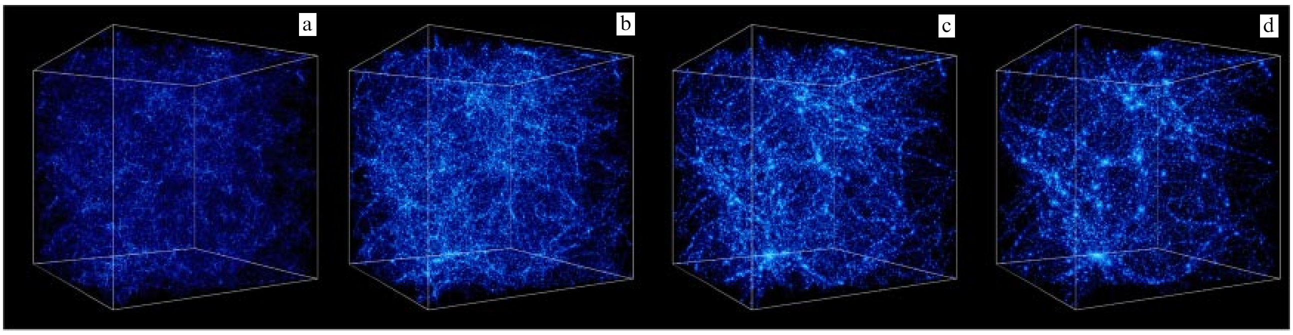

Figure 3. Spatial distribution of dark matter in numerical simulations of structure formation in the CDM model with the cosmological constant in a cubic comoving volume with a size of 85 Mpc [56] in four epochs: (a) $z = 8$, (b) $z = 4$, (c) $z = 1$, and (d) $z = 0$.

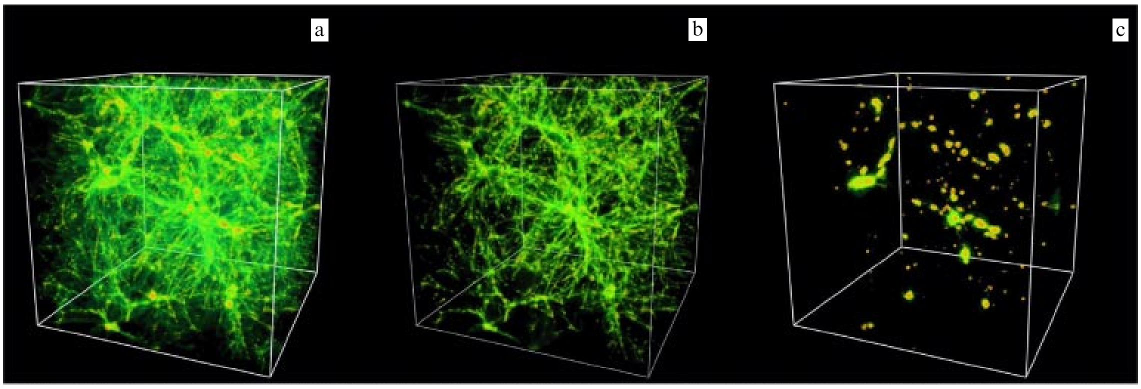

Figure 4. (Color online) Spatial distribution of diffusive baryonic gas in hydrodynamic simulations of the structure formation in the CDM model with the cosmological constant [60]. The simulated cubic volume has a size of 100 Mpc, close to the volume shown in Fig. 3. (a) The space rendering of the total volume gas distribution. The color corresponds to the gas density contrast relative to the mean baryonic density in the Universe; the density contrast ~ 10, ~ 100, and $\gtrsim 1000$ is respectively shown in green, yellow, and red. (b) Only baryons with a temperature $10^5 < T < 10^7$ K. (c) Only baryons with a temperature $> 10^7$ K. It can be clearly seen that gas in filaments has an intermediate temperature $T \sim 10^6$ K, and the hottest plasma is concentrated in quasi-spherical condensations corresponding to galaxy clusters.

[59–61]. This hot phase was recently discovered in observations [62] from cross-correlating the projected mass distribution, measured by the weak gravitational lensing method and from the Sunyaev–Zeldovich (SZ) effect [63, 64] measured by the Planck space observatory.

In addition to the large-scale structure, many dense collapsed halos can be seen in Fig. 3. The halos correspond to minima of the potential, around which normal matter should be accumulated to form galaxies in the course of the cooling of gas heated by the shocks [65]. Galaxy formation is accompanied by a number of complex processes, in which the cooling and condensation of the baryonic gas can lead to compression of dark matter in the halo centers (Fig. 4) [66–68] and change of the halo shape to a more spherical one [69]. The energy released by young massive stars as electromagnetic radiation and kinetic energy of stellar winds, as well as shocks and cosmic rays due to supernova explosions, can subsequently lead to ejection of most of the condensed baryonic gas from the halo and to a decrease in the central dark matter density.

Numerical modeling of these complicated phenomena is very topical because it is already clear that understanding these processes is crucial for progress in explaining the general picture of galaxy formation. Here, simulations of galaxy clusters play a special role for two reasons (see, e.g., a detailed review in [70]). First, the clusters are unique astrophysical laboratories in which all matter constituents are observed. For example, the distribution of stars and cold gas is studied by panchromatic observations from UV to IR and radio bands. The mass distribution and thermodynamic properties of the hot gas are investigated by X-ray observations (see, e.g., [71]) and via the SZ effect [63, 64, 72]. The distribution of dark matter is probed by measuring galactic velocities [73] and by gravitational lensing [74]. Second, the clusters play an important role as cosmological 'beacons' of structure formation (see, e.g., the recent detailed review [75] and Section 3 below).

2.4 Modeling the galaxy cluster mass function

The time and rate of the collapse of any density peak is determined by its initial amplitude, the gravitational attraction force at the corresponding scale, and the expansion rate of the Universe that counteracts the gravitational attraction and decelerates the collapse. The epoch of massive cluster formation occurs at $z \lesssim 2$, and the spatial density of these clusters at various redshifts, depending on the mass (mass function), is very sensitive to the normalization of the perturbation spectrum, to the Universe's expansion rate, which is dependent on the mean density of matter and dark energy, and to the properties of the gravity law on the largest scales [70].

These dependences are calibrated using numerical simulations of structure formation. However, in addition to using the calculations, a number of analytic models of the cluster mass function have been elaborated, which are useful in both interpreting the results of numerical simulations and understanding the origin of the cluster mass function dependence on the properties of initial perturbations and cosmological parameters.

The first statistical model of the mass function of collapsed density peaks was developed in [76]. The model is based on the assumption that the mass function is directly related to the statistical properties of primordial density perturbations, such as the power spectrum $P(k)$. For example, the probability $F(M)$ that a given region with the initial density contrast $\delta_M(\mathbf{x}) \equiv \rho(\mathbf{x})/\bar{\rho} - 1$, where $\bar{\rho}$ is the mean density of matter and the density field $\rho(\mathbf{x})$ is smoothed on the mass scale M (corresponding to the space scale $R \approx [3M/(4\pi\bar{\rho})]^{1/3}$), collapses into an object with a mass $\geqslant M$ is expressed as

$$F(M) = \int_{-1}^{\infty} p(\delta) C_{\text{coll}}(\delta)\, \mathrm{d}\delta\,. \tag{3}$$

Here, $p(\delta)\,\mathrm{d}\delta$ is the probability distribution $\delta_M(\mathbf{x})$, usually assumed to be Gaussian, and C_{coll} is the probability that a given point $\mathbf{x}$ in space with a contrast $\delta_M(\mathbf{x})$ collapses. In this case, the mass function of the collapsed objects with a mass in the interval $(M, M + \mathrm{d}M)$ is equal to $\mathrm{d}F/\mathrm{d}M$ divided by the comoving volume of the initial density perturbation field, occupied by regions of the mass M, i.e., $M/\bar{\rho}$:

$$\frac{\mathrm{d}n(M)}{\mathrm{d}M} = \frac{\bar{\rho}}{M} \left| \frac{\mathrm{d}F}{\mathrm{d}M} \right| . \tag{4}$$

In the Press–Schechter approach [76], the model of collapse of a spherically symmetric perturbation with constant density was used [77], in which the perturbation collapses when the linear density contrast reaches the critical value [4] $\delta_c \approx 1.69$. Based on this result, Press and Schechter postulated that any point with a density contrast $\delta_M(\mathbf{x}) D_{+0}(z) \geqslant \delta_c$ would collapse into a halo with a mass $\geqslant M$ before the redshift z, i.e., $C_{\rm coll}(\delta) = \Theta(\delta - \delta_c)$, where Θ is the Heaviside step function. Importantly, the contrast $\delta_M(\mathbf{x})$ in this context is the initial contrast, linearly extrapolated to the epoch z using the linear perturbation growth function $D_{+0}(z)$ normalized such that $D_{+0}(0) = 1$. It is easy to verify that for a Gaussian initial perturbation field, this assumption yields $F(M) = (1/2)\,\mathrm{erfc}\,[\delta_c/(\sqrt{2}\sigma(M,z))] = F(\nu)$, where $\sigma(M,z)$ is the dispersion of the contrast density field smoothed on the scale M and linearly extrapolated to the redshift z, and $\nu \equiv \delta_c/\sigma(M,z)$ is the so-called peak collapse amplitude. The quantity ν characterizes the amplitude of collapsing density peaks in units of the density field dispersion. The mass function per unit logarithmic mass interval in this model is expressed as

$$\frac{\mathrm{d}n(M)}{\mathrm{d}\ln M} = \frac{\bar{\rho}}{M}\left|\frac{\mathrm{d}F}{\mathrm{d}\ln M}\right| = \frac{\bar{\rho}}{M}\left|\frac{\mathrm{d}\ln\nu}{\mathrm{d}\ln M}\frac{\partial F}{\partial \ln\nu}\right| \equiv \frac{\bar{\rho}}{M}\left|\frac{\mathrm{d}\ln\nu}{\mathrm{d}\ln M}\right| g(\nu) \equiv \frac{\bar{\rho}}{M}\,\psi(\nu)\,. \qquad (5)$$

Later research showed that the form of the function $\psi_{\rm PS}(\nu)$ predicted by the Press–Schechter model is not very accurate: the difference between the numerically simulated mass function and the actual cluster mass function reaches 50% for some masses [79–83]. In principle, we can expect some inconsistencies simply due to differences between the cluster mass definition in the model and numerical simulations. In the model, the mass is determined by the filter used to smooth the density field, whereas in numerical calculations, the mass is determined either inside the density contour corresponding to a certain density contrast or inside a spherical region in which the density is equal to a certain contrast relative to the mean density of matter or to the critical density of the Universe, $M = (4\pi/3)\Delta\rho_r R^3$, where $\rho_r = \bar{\rho}(z)$ or $\rho_r = \rho_{\rm crit}(z)$, and typically $\Delta \sim 200-500$ is used (see [70, § 3.6] for a more detailed discussion of the cluster mass definition). However, the difference in mass definition is not the main source of errors.

In fact, it is quite easy to see that in the Press–Schechter formalism, the form of the function $\psi(\nu)$ directly depends on the assumed collapse model of density peaks. As noted above, the typical peaks in a Gaussian density field have an ellipsoidal shape, and their collapse is therefore anisotropic and cannot be accurately described by the spherical collapse model. Models based on the same general approach but with the function $C_{\rm coll}$ calculated using the anisotropic collapse of perturbations were developed in the second half of the 1990s [42, 82, 84, 85]. For example, the Sheth–Mo–Tormen model involves the statistics of the shape of density peaks in a Gaussian field, with each peak approximated by an ellipsoid using ellipsoid collapse models [86, 87]. The Lee–Shandarin model [42], however, involves the Zeldovich approximation to directly calculate the collapse of peaks, which is characterized by local eigenvalues of the deformation tensor. Figure 5 demonstrates that both these models predict the cluster mass function in much better agreement with numerical simulations than the Press–Schechter model does, especially for masses corresponding to groups and clusters of galaxies ($\nu \gtrsim 1$). The accurate calibration of the mass function for the largest masses is still going on [89, 90], although currently the accuracy is already limited by uncertainties of physical processes in the baryonic matter related to galaxy formation [91–93].

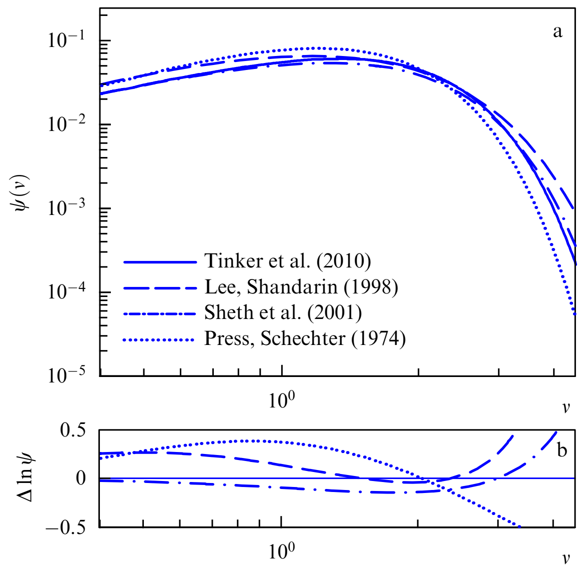

Figure 5. (a) Dependence $\psi(\nu)$ on the peak amplitude ν, which determines the mass of collapsed objects $\mathrm{d}n/\mathrm{d}\ln M = \bar{\rho}\psi(\nu)/M$ [see Eqn (5)] as a function of the peak amplitude, as predicted in the Press–Schechter model (dotted curve), in the Lee–Shandarin model [42] based on the Zeldovich approximation (dashed line), and in the Sheth–Mo–Tormen model [86] (dashed-dotted line), and as obtained in numerical simulations (the solid line) [88]. (b) Deviations of the model result from numerical calculations.

The Press–Schechter model, nevertheless, played a major role in showing that the *mass function of objects at different redshifts can be a universal function of the density peak amplitude*, $\nu(M,z) \equiv \delta_c/\sigma(M,z)$. In particular, the form of $\psi(\nu)$ mainly depends on the physics of the density peak collapse and not on the cosmological model parameters. This gave impetus to both elaborating more sophisticated models based on the Press–Schechter formalism [5] and the productive analysis of numerical simulations by revealing that the calibration of $\psi(\nu)$ in one cosmology can work well in other cosmologies [83, 101, 102].

Figure 5 demonstrates that for masses corresponding to $\nu \lesssim 2$, the function $\psi(\nu)$ weakly changes with changing ν, which corresponds to the mass function $\mathrm{d}n/\mathrm{d}M \propto M^{-\alpha}$ with $\alpha \approx -1.8-1.9$ [see Eqn (5)]. But for $\nu \gtrsim 2$, $\psi(\nu)$ rapidly (exponentially) decreases with increasing ν. Massive galaxy clusters have exactly such peak amplitudes, and their mass function depends exponentially on the mass and the cosmological parameters on which ν depends. It is this exponential sensitivity to cosmological parameters that makes the clusters invaluable for cosmological studies. At the same time, the exponential dependence on the mass M implies that when comparing the observed cluster sets with theoretical predictions, special attention should be given to measuring the mass M.

[4] This critical density contrast formally depends on cosmological parameters (see, e.g., [78]). However, this dependence is rather weak.

[5] In recent decades, a number of such models have been developed, which can describe the numerical simulations more accurately due to introducing new free parameters and additional assumptions (see, e.g., [94–100]).

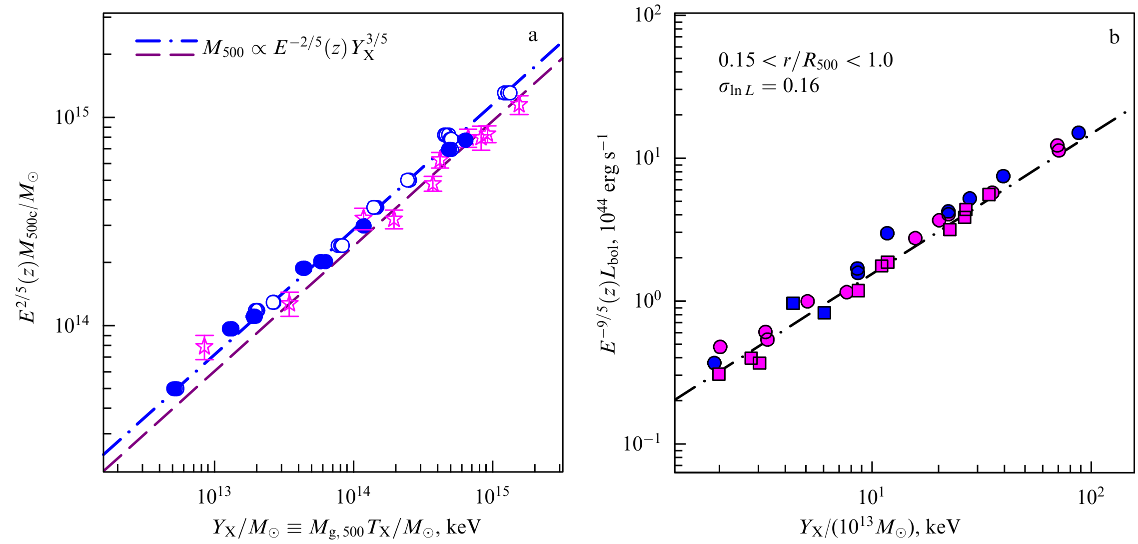

Figure 6. (Color online) (a) Relation between $Y_X = M_{gas} T_X$ and the total mass $M_{500} = M(r < R_{500})$. Circles display clusters in numerical simulations [111], stars with errors show observed clusters for which the value of Y_X is derived from X-ray Chandra observations and the total mass is inferred from X-ray data by assuming a hydrostatic equilibrium [71]. The filled dots correspond to clusters with regular X-ray images without visible signatures of recent merging and dynamical interactions. The dashed-dotted and dashed lines correspond to power laws with the exponent $\alpha = 3/5$ that describes the cluster properties in numerical simulations and observations; $E(z) = H(z)/H_0$ [where $H(z)$ is the Hubble constant at a redshift z], M_{500c} is the mass of the cluster within a sphere whose mean density exceeds the critical density in the Universe, and $M_{g,500c}$ is the gas mass inside this sphere. (b) The relation between Y_X and the bolometric luminosity L_{bol} of hot intergalactic cluster gas as measured by the XMM-Newton (X-ray Multi-Mirror Mission Newton) observatory [112]. The luminosity measurements were performed for the region inside the radius R_{500}, with a contribution from the central cluster part, with $r < 0.15 R_{500}$ excluded. The blue symbols show the clusters with bright X-ray cores (so-called cooling cores). The pink symbols mark the clusters with less bright cores. Clusters without traces of dynamical interactions are shown by dots, and those with such signatures are shown by squares; $\sigma_{\ln L}$ is the rms deviation of the luminosity logarithm ($\ln L$) from the mean power-law dependence.

2.5 Measuring the total masses of clusters and their mass function

As we have seen, the cluster mass estimate is the key issue for cosmological applications. Theoretically, the total masses of individual clusters can be quite accurately estimated by assuming hydrostatic equilibrium and derived from X-ray observations (see, e.g., [71]) or from analyzing gravitational lensing of background galaxies by the cluster (see, e.g., [103, 104] and the recent pedagogical review [74]), but in practice these measurements are often difficult when done for large samples of objects due to their complexity or limited application. For example, the hydrostatic equilibrium estimate is inaccurate for clusters that recently merged with another cluster [105–109]. Numerical cosmological simulations also show that the masses estimated from weak lensing for some clusters have a significant dispersion relative to the mass used in theoretical calibrations of the mass function [110].

In practice, therefore, an observed cluster property is chosen such that, on the one hand, it can be reliably measured from observational data, and on the other hand, it correlates with the mass with a small dispersion. Such properties can be deduced from numerical simulations of galaxy clusters. These simulations usually cannot predict the exact form of correlations, because their results are sensitive to still uncertain physical processes involved in galaxy formation, which strongly affect most observational properties of stars and the intergalactic gas in the clusters. Nevertheless, the simulations can rather confidently predict the dispersion of correlations of different observables and of the total mass of clusters, as well as their sensitivity to various uncertain galactic processes and the evolutionary stage of the clusters.

Figure 6 shows an example of numerical simulation results used to choose optimal observables as cluster mass indicators. For example, numerical simulations revealed that the total internal energy of the hot gas in clusters comprised inside the region with a sufficiently large radius R, $E_{th} = \int_{r<R} n_e T_e \, dV$, where n_e and T_e are the density and temperature of electrons in the hot cluster plasma, shows minimal dispersion relative to the cluster mass [113, 114]. This energy is linked to the integral amplitude of the SZ effect [63, 64] inside the corresponding volume, $Y_{SZ} = (k_B \sigma_T / m_e c^2) E_{th}$, which is determined by the observables of these effects in clusters[6] (see, e.g., detailed review [72]).

Although observational errors of the SZ effect measurements still preclude mass estimates from reaching the theoretically expected accuracy, a similar indicator can be obtained from X-ray cluster measurements [111]. This quantity is simply the product of the gas mass and temperature averaged over the interval of radii, excluding the cluster core: $Y_X = M_g T_X$.

The analysis of numerical simulations reveals that if the temperature is estimated in the range of radii $0.15 < r/R_{500} < 1$, where R_{500} is the radius of the region inside which the total mass density is equal to $500\rho_{crit}(z)$ and $\rho_{crit}(z)$ is the critical density of the Universe at the observed redshift, then Y_X correlates with the total mass of the cluster inside the radius R_{500} with a dispersion of only $\approx 8\%$, as shown in Fig. 6a. Moreover, the slope of this power-law correlation and its dispersion are virtually insensitive to the uncertain processes related to galaxy formation and to the dynamical state of the cluster [111, 115–117].

[6] Here k_B, σ_T, m_e, and c are the Boltzmann constant, the Thomson cross section, the electron rest mass, and the speed of light.

Although the temperature must be measured to determine Y_X, Fig. 6b indicates that the bolometric luminosity of clusters, measured inside the radius range $0.15 < r/R_{500} < 1$ for the observed sample of clusters with different properties and dynamical states [112], has a dispersion of only $\approx 16\%$ relative to Y_X. The gas mass inside the region with the radius R_{500}, tightly connected with the X-ray luminosity shown in Fig. 6, has a dispersion of only $\approx 5-8\%$ relative to Y_X and the total mass of the clusters [111, 117]. Hence, the values with a relatively low dispersion relative to the mass can also be derived from those X-ray observations in which the temperature cannot be measured. However, in that case, the correlation slope is much more sensitive to the details of physical processes related to galaxy formation and to uncertainties in the numerical modeling of these processes [117].

Quantities similar to Y_X, the mass of gas, and the cluster luminosity (excluding contributions from the inner parts) are now widely used to estimate the galaxy cluster mass function at different redshifts. These estimates and their application to constraining cosmological parameters, including the dark energy density, are discussed at length in Section 3.

3. Cosmological studies with galaxy clusters

Theoretical arguments and results of numerical simulations described in Section 2 reveal a strong dependence of cluster properties on the cosmological model. Therefore, galaxy cluster studies allow imposing stringent constraints on several critically important parameters, for example, on the empirical description of so-called dark energy, which is responsible for the accelerated expansion of the Universe [118, 119].

There are two principal observational manifestations of dark energy. One is due to the dark energy effect on the expansion of the Universe as a whole. The dependence of the expansion factor on time can be derived from the distance–redshift relation, measured, for example, using type-Ia supernovae as standard candles, or the baryonic acoustic oscillation wavelength (see, e.g., [18, 120]) as the standard ruler [121]. This type of cosmological measurement is usually referred to as 'geometrical'.

The other potentially observable effect is the dark energy influence on the large-scale structure growth rate. It is expected that the structure growth rate slows after the Universe starts the accelerating expansion at $z \approx 0.8$. If the value of this effect is measured with sufficient accuracy, for example, from the Sachs–Wolf effect [122], from weak gravitational lensing on large-scale structures, from distortion of the radial projection of galaxy distribution [123], or from galaxy cluster evolution, as discussed below, then, combined with geometrical methods, this must significantly improve the accuracy of the determination of dark energy characteristics [121]. In addition, the possibility arises of checking the validity of general relativity (GR) equations at large scales, 10–100 Mpc [124].

We note that galaxy cluster observations offer the possibility of probing structure growth in the Universe and of performing geometrical tests. Observations of individual clusters allow determining the distant–redshift relation either through the SZ effect [125], by combining microwave and X-ray data for a particular object, or by using the expected universality of the specific fraction of the hot intergalactic gas, $f_{gas} = M_{gas}/M_{tot}$ [126, 127]. These methods can be

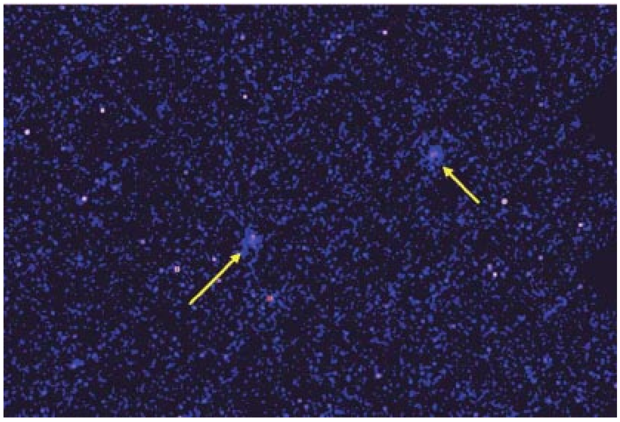

Figure 7. Example of using an X-ray image to search for distant galaxy clusters. This sky area was observed by Chandra for 1.5 hours. The extended X-ray emission of the intergalactic gas in two clusters (marked with arrows) is clearly distinguished on the statistical noise background and numerous point-like sources.

applied to independently measure the Hubble constant by observing clusters at small z.

Measurements of the structure growth rate using clusters are currently performed mainly based on the cluster mass function, whose amplitude is exponentially sensitive to the linear amplitude of matter density perturbations at a given redshift, and hence allows deriving exact constraints even in the case of relatively poor object samples [128].

In the near future, the availability of huge cluster catalogs ($\sim 10^5$ objects), which can be found, for example, from the deep X-ray survey of the SRG observatory,[7] will enable two additional cosmological tests. First, in such extensive catalogs, it will be possible to detect baryonic oscillations in the spatial distribution of objects, to provide an independent geometrical test. Second, the structure growth can be traced not only by the cluster mass function evolution but also by the gradual increase in its spatial correlation amplitude.

The practical possibility of precise cosmological measurements using galaxy clusters arose after the launch of the Chandra and XMM-Newton X-ray observatories, which yielded detailed data for individual objects (Fig. 7). Simultaneously, significant progress was made in theoretical and numerical cluster modeling (see, e.g., [129]). This led to a deeper understanding of physical processes in clusters and a dramatically improved possibilities of obtaining reliable mass estimates from observations. In the last few years, the elaborated methodology has been used to measure the cosmological model parameters with next-generation sky surveys based on the SZ effect.

3.1 Galaxy cluster catalogs with high statistical 'purity'

The first precise cosmological results with galaxy clusters were obtained using catalogs of distant objects found in images by the ROSAT satellite (from the German, Roentgensatellit). The experience from this research is extremely important for the future SRG observatory that will be able to survey the entire X-ray sky with the sensitivity and angular resolution that were attained by ROSAT only in observations of a small area of about 100 square degrees.

The ROSAT X-ray observatory, operated in the 1990s, provided extensive data for sampling galaxy clusters at

[7] http://hea.iki.rssi.ru/ru/index.php?page = srg.

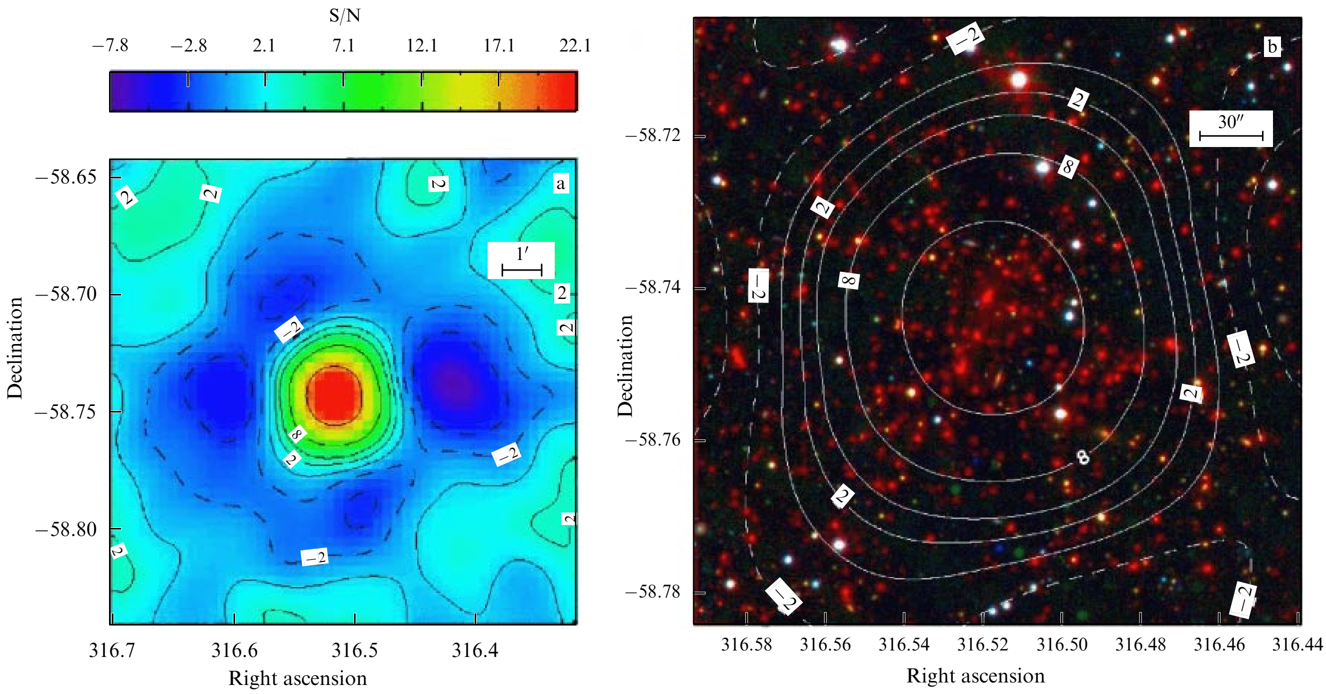

Figure 8. Example of detecting a remote galaxy cluster ($z = 1.1$) using the SZ effect [135]: (a) image taken by SPT (S/N is the signal-to-noise ratio), and (b) optical image.

redshifts up to $z > 1$ with high statistical completeness [130]. The ROSAT satellite conducted X-ray surveys with different sky coverage in a wide sensitivity range (see, e.g., the BCS (Bright Cluster Sample) and REFLEX (ROSAT-ESO Flux-Limited X-ray Survey) catalogs [131, 132]). Due to 'heroic' efforts on optical identification, the all-sky ROSAT survey can be used to search for record large clusters at redshifts up to $z \sim 0.5$ (see MACS (Massive Cluster Survey) [133]). In the X-ray pointing regime, ROSAT covered only about 2% of the sky at high galactic latitudes. But the sensitivity and angular resolution in this regime were much higher than during the all-sky survey, which allowed these data to be used in searching for clusters at $z \approx 0.6$ in approximately the same mass range where the all-sky survey was sensitive to small objects at low z. One of the most well-known and widely exploited cluster catalogs is the so-called 400d catalog [134], comprising 266 clusters and galaxy groups with the maximum $z = 0.9$, compiled from the analysis of a large number of ROSAT X-ray images taken in the pointing regime with a total coverage of 400 square degrees.

Recently, the focus of searches for distant galaxy clusters and their use in cosmology has shifted to studies relying on the SZ effect (Fig. 8). Experimental searches for clusters are being carried out using sky maps obtained by the Planck satellite, as well as using sensitive surveys of areas several thousand square degrees in size obtained by the ground-based telescopes SPT (South Pole Telescope) and ACT (Atacama Cosmology Telescope) [135–137]. Due to the large coverage area and the weak redshift dependence of the observed effect, the Planck, SPT, and ACT surveys have significantly extended the cluster mass function measurements toward higher masses and higher z.

3.2 Detailed measurements of individual object parameters

In spite of the rapid development of instruments aimed at observing the SZ effect, X-ray data continues to provide the most accurate measurements of individual galaxy parameters. X-ray observations of low-redshift objects by Chandra and XMM-Newton are able to measure the density, temperature, and metallicity profiles of hot cluster gas in detail in a wide interval of radii. A range of systematic studies [138–140] reveals a general picture in which the hot gas properties demonstrate a high degree of self-similarity (Fig. 9, 10) (see also [141, 142]) outside the central parts of the cluster, where the processes that are not directly related to the intergalactic gas heating during gravitational collapse are important (see Section 5).

Such measurements of the cluster characteristics are extremely important for cosmological applications. First, they provide dependences necessary for measuring the cluster mass profile by one of the most popular methods, based on the hydrostatic equation of a gas in a spherically symmetric gravitational field. Second, the observed hot gas profiles are extremely valuable for testing the accuracy of numerical simulations of cluster formation [8] (see Section 5). Finally, the self-similarity of the observed hot gas profiles directly suggests that the cluster properties are mainly determined by a single parameter, their total mass. This is the key feature of the theory of galaxy cluster formation and underlies the use of these clusters in cosmology.

3.3 Cluster mass measurements

Although the existence of self-similar relations between different properties of galaxy clusters and their total mass

[8] We note that at the current level of theory and observational accuracy, numerical simulations cannot be used for exact predictions of galaxy cluster properties in different cosmological models by considering their evolution from the initial conditions in the early Universe. The numerical simulations play the leading role in justifying the existence of relations between the total mass of objects and their observed integral X-ray and SZ properties. These predictions are reliable insofar as we can check that the numerical models correctly reproduce even more complicated and nontrivial properties of galaxy clusters.

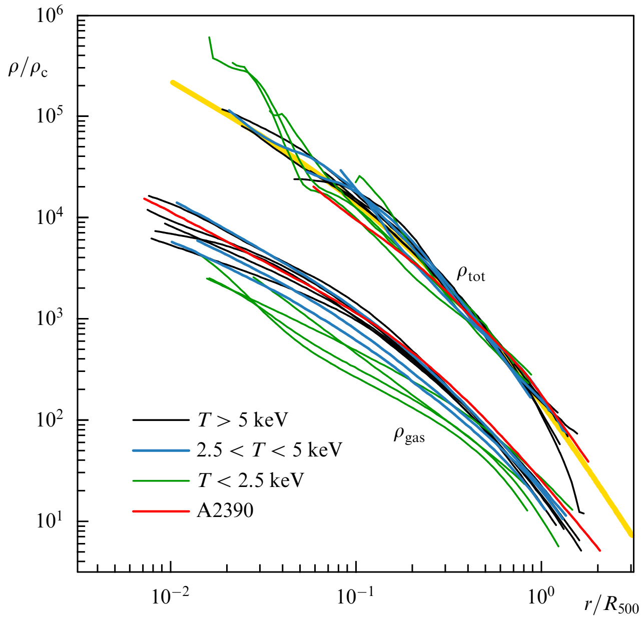

Figure 9. Scaled density profiles of all cluster matter ρ_{tot} and of the hot gas ρ_{gas} as measured by the Chandra observatory [138].

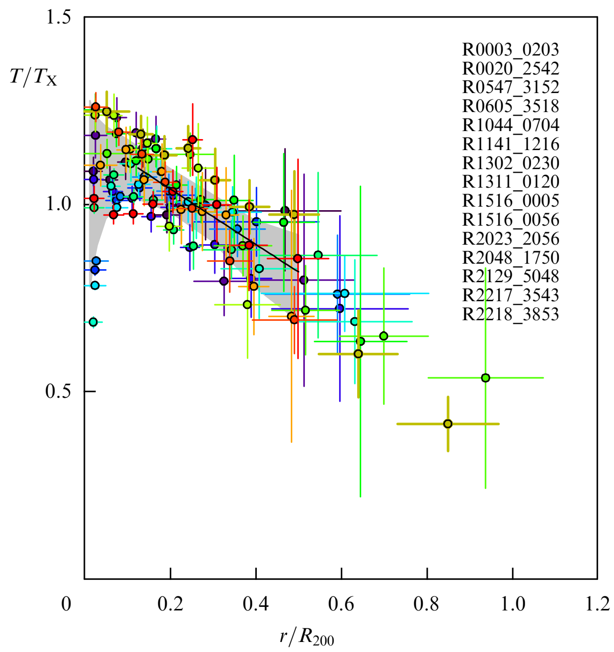

Figure 10. Scaled temperature profiles of the hot gas in a representative cluster sample as measured by the XMM-Newton observatory [140].

has been recognized, the absolute link of these relations to the total mass of objects was uncertain for a long time (see, e.g., a review of the situation in 2003 from the theoretical standpoint in [143]).

Today, the situation is much better [144]. The normalizations of relations between the cluster masses and their parameters obtained from X-ray mass measurements in dynamically 'quiet' objects (see, e.g., [138]), as inferred from numerical simulations [145, 146] and from gravitational lensing observations of representative samples [145, 146], are consistent up to about 10%. This accuracy is sufficient for a range of cosmological parameter measurements. The ten-percent accuracy of the absolute calibration of cluster masses follows not only from comparing different measurement methods but also from the implicit consistency of the cosmological parameters derived from X-ray observations [147] and from analyses of optically selected clusters with their subsequent mean mass calibration using the gravitational lensing method [148], as well as from recent measurements of the weak gravitational lensing effect in large sky areas [149].

3.4 Geometrical test using X-ray data and the Sunyaev–Zeldovich effect

As mentioned above, SZ observations of the hot gas in galaxy clusters are becoming comparable in accuracy with the best X-ray measurements of the gas characteristics. Because the X-ray signals and SZ signals depend on the distance to the object differently, the possibility arises of measuring the cosmological distance–redshift relation and comparing these data.

Presently, the most interesting results obtained by this method include measurements of the absolute distance to a range of galaxy clusters, which yield an independent value of the Hubble constant, $H_0 = 76.9 \pm 10$ km s^{-1} Mpc^{-1} [150].

3.5 Geometrical test using the hot gas specific mass fraction f_{gas}

It is expected in [151] that on galaxy cluster scales, gravity is the main force, and therefore baryons and dark matter should not be significantly separated in the course of cluster formation; hence, the baryon fraction in the total cluster mass should be close to the mean value in the Universe, $f_b = M_b/M_{tot} \approx \Omega_b/\Omega_M$. The expected universality of f_b can be used as a distance measure as follows [126, 127].

The mass of the hot gas (about 80%–90% of the total baryonic mass [152]), as derived from X-ray data, is proportional to $d^{5/2}$, where d is the distance to the cluster. The total mass inferred from the hydrostatic equilibrium equation or any other dynamical method scales as d. Therefore, the hot gas fraction in the total cluster mass, derived from observations, is proportional to $d^{3/2}$ and is constant as a function of z only when the correct distance–redshift relation is used.

The practical application of this cosmological test became possible only after the launch of the Chandra X-ray observatory in 1999. The results of the test independently support the conclusion that the current evolution of the Universe is primarily governed by dark energy (Fig. 11). The expected constancy of measured f_{gas} at different z is indeed observed for a combination of cosmological parameters around $\Omega_M = 0.3$ and $\Omega_\Lambda = 0.7$, whereas, for example, the combination $\Omega_M = 1, \Omega_\Lambda = 0$ leads to strong trends in $f_{gas}(z)$.

Unfortunately, using this method for more precise cosmological estimates is difficult because f_{gas} (and even the total baryon fraction, comprising stellar matter in galaxies) is not exactly constant, which appears in the observed trends of f_{gas} with changing radius in individual objects, as well as in the dependence of f_{gas}, measured within a fixed fraction of the virial radius, on the total mass of the object [138, 139, 142]. The presence of these trends in low-z clusters almost certainly implies that the 'true' value of f_{gas} should also vary with the redshift.

Unfortunately, theoretical cluster models are insufficiently developed for precisely accounting for effects that are can be responsible for the incomplete universality of the value f_{gas}. Hence, in practical applications of the cosmological test based on $f_{gas}(z)$, a significant level of systematic uncertainties

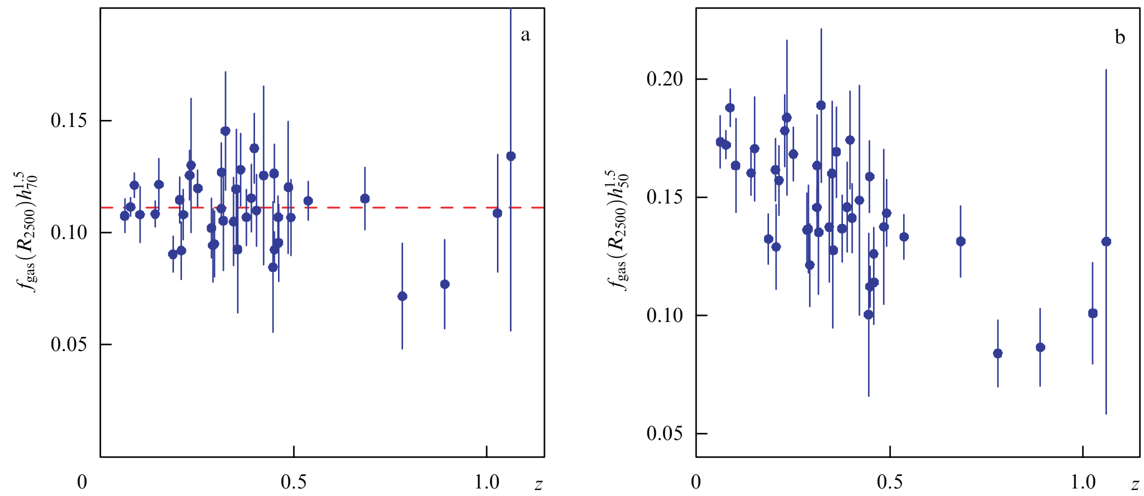

Figure 11. A realization of the cosmological test $f_{\rm gas}(z)$ using the Chandra X-ray data [153]. (a) The values of $f_{\rm gas}$ obtained by assuming the 'standard' ΛCDM cosmology, as expected, do not demonstrate strong trends with z. (b) The same measurements, assuming an 'incorrect' cosmological model with the deceleration parameter $q_0 = 0.5$, produce a strong, easily detectable trend. h_{50} (h_{70}) is the Hubble constant normalized to 50 (70) km s^{-1} Mpc^{-1}.

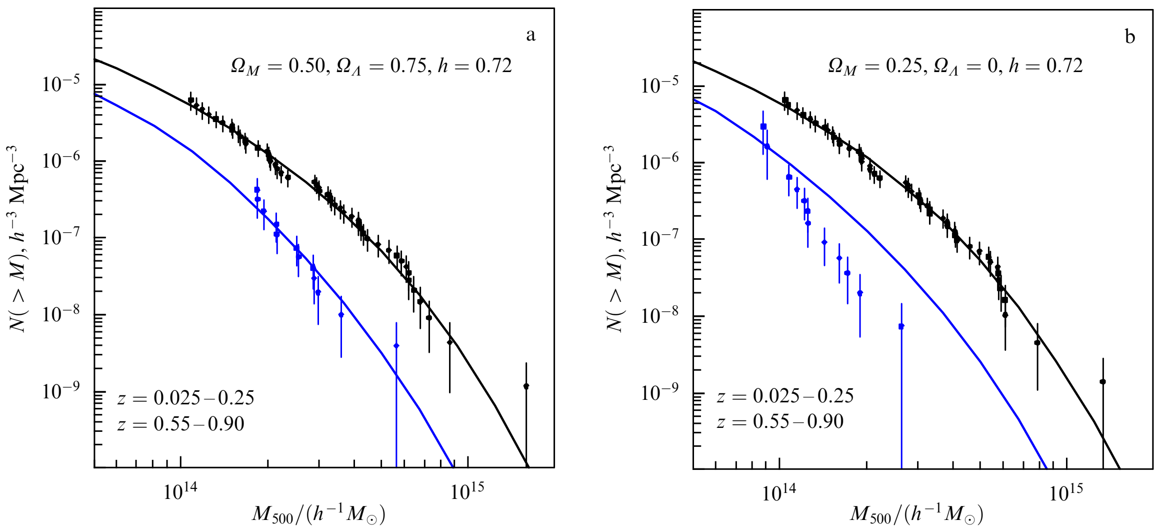

Figure 12. Sensitivity of the cluster mass function to cosmological parameters. (a) Mass function measurements and theoretical predictions for cosmological parameters close to the commonly recognized values; N is the cumulative mass function and h is the normalized Hubble constant. (b) The data and theoretical prediction obtained for a cosmological model with $\Omega_\Lambda = 0$. In this case, after normalizing the theoretical curves to the measurements, at low z, a strong disagreement is seen at $z > 0.55$, suggesting that this combination of Ω_M and Ω_Λ should excluded.

should be taken into account, which restricts the accuracy of the method for determination, for example, of the state parameter in the dark energy equation (see, e.g., [153]).

3.6 Measuring the large-scale structure growth rate

The growth rate of structures in the Universe is a beautiful addition to the distance–redshift tests (see,e.g., [154]) and has a comparable sensitivity to the dark energy properties. The cluster mass function evolution traces the general growth of the small matter density perturbations, but with an exponential enhancement. Therefore, an acceptable accuracy level in determining the cosmological parameters is achievable from the analysis of relatively poor samples of the objects.

Currently, the best measurements of the galaxy cluster mass function from X-ray data allow tracing the perturbation growth history in the redshift range $z = 0-0.7$. The results of these measurements confirm the deceleration in the perturbation growth rate due to transition to the accelerated expansion stage. They also greatly improve constraints on the effective parameter of the dark energy equation of state and even set an upper bound on a 'nonstandard' gravitational interaction on scales ~ 10 Mpc in some model GR extensions.

Figure 12 illustrates the sensitivity of the galaxy cluster mass function to the presence of dark energy. The cluster sample used in [147] is statistically representative enough to measure the density perturbation amplitude at redshifts $z = 0.015-0.150,\ 0.35-0.45,\ 0.45-0.55$, and $0.55-0.90$. By combining these results with the fluctuation amplitude at $z \approx 1000$, as derived from the angular CMB anisotropy, it is possible to reconstruct the perturbation growth history in a very broad redshift range (Fig. 13). These data clearly

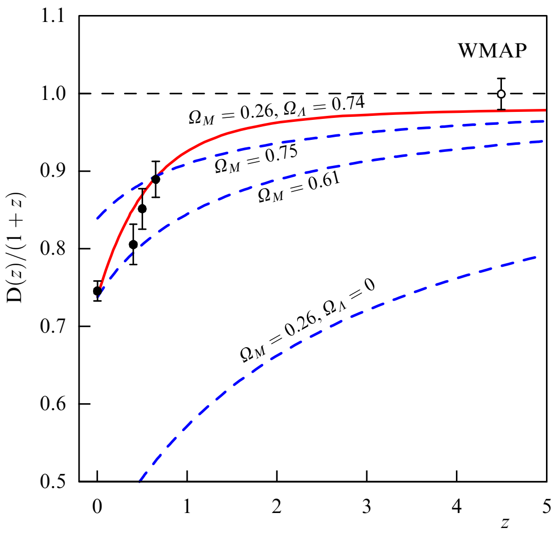

Figure 13. Evolution of the relative amplitude of linear matter density perturbations in the Universe derived from the cluster mass function (black dots). The total amplitude of this dependence is normalized to its value at $z \approx 1000$, inferred from WMAP measurements of CMB fluctuations (the white dot, conventionally set to $z = 4.5$), and to the growth rate that is expected in the cosmological model with $\Omega_M = 1$ without dark energy. (WMAP, Wilkinson Microwave Anisotropy Probe.) The solid line displays the growth rate that is expected in the 'standard' ΛCDM model, and the dashed lines indicate the growth rate in models without dark energy with different values of the parameter Ω_M.

demonstrate the perturbation growth deceleration at low z. The data also suggest that the transition to a slower growth occurred fairly close to $z \sim 1$, exactly as expected in cosmological models with dark energy.

3.7 Expected results of future experiments

In the coming years, a precise measurement of galaxy cluster properties is expected at different wavelengths. In addition, space and ground-based experiments aimed at conducting large-area sky surveys will produce galaxy cluster catalogs comprising several tens and hundreds of thousands of objects in a wide range of masses and redshifts. This will significantly improve the precision of the cosmological tests discussed above. We consider several examples.

The most significant progress is expected from the SRG space observatory (scheduled to launch in 2016), which will produce a catalog of 10^5 galaxy clusters selected by the 'purest' of the existing methods, X-ray emission of intergalactic gas. The sensitivity of the SRG surveys will be sufficient to discover all clusters inside the visible Universe above a threshold mass $M_{500} \sim 3 \times 10^{14} M_\odot$.

The results of the second year of observations of the Planck observatory, as well as of the sky surveys conducted by the upgraded ACT and SPT telescopes, will significantly increase the number of galaxy clusters with a precisely measured SZ effect. These experiments will probably not match the SRG in the total number of detected objects. However, the simultaneous X-ray and microwave measurements of the hot gas parameters in clusters increase the accuracy and reliability of cosmological measurements.

Significant progress in precise measurements of cluster parameters is also expected due to optical sky surveys, such as DES (Dark Energy Survey) currently ongoing for the second year and the Euclid satellite survey scheduled for launch in 2019, as well as the infrared sky survey to be conducted by the WFIRST (Wide-Field Infrared Survey Telescope) satellite scheduled for launch in the first half of the 2020s. The optical and infrared surveys will also result in extensive (several hundred thousand) catalogs of clusters, selected from the analysis of galaxy color distribution and in the sky projection. This method of cluster searches is less pure than using X-ray emission or the SZ effect from hot intergalactic gas; however, the catalogs obtained may be used for qualitative measurements of the spatial distribution of clusters and for performing related cosmological tests.

An absolutely new possibility that is opened up by new-generation optical and infrared surveys is measuring the mean signal from weak lensing from several hundred and thousands of galaxy clusters, leading to a dramatic improvement in the absolute precision of the cluster mass calibration.

4. Shocks in the intergalactic gas

According to the modern picture of the growth of the large-scale structure in the Universe, galaxy clusters result from the merging of less massive clusters and groups due to gravitational attraction. Later on, many of them merge with larger clusters; the largest modern structures that have reached virial equilibrium have masses about $10^{15} M_\odot$. Examples of clusters at different stages of this hierarchical assembly are displayed in Fig. 14.

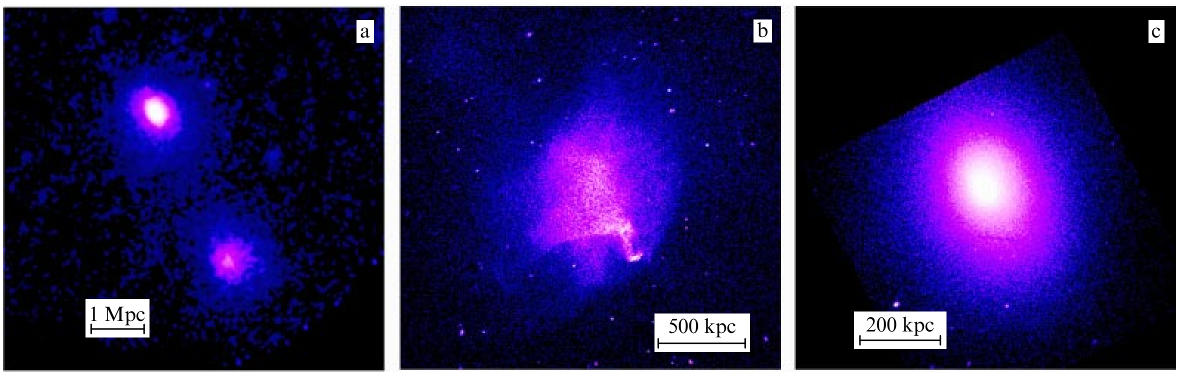

Figure 14. (a, b) X-ray images of clusters at different stages of merging. (a) A pair of clusters approaching each other (A401-A399, ROSAT). (b) The collision and strong perturbations in the intergalactic medium, including a shock wave (A520, Chandra). (c) The final result in a state close to the hydrodynamic equilibrium (A2029, Chandra).

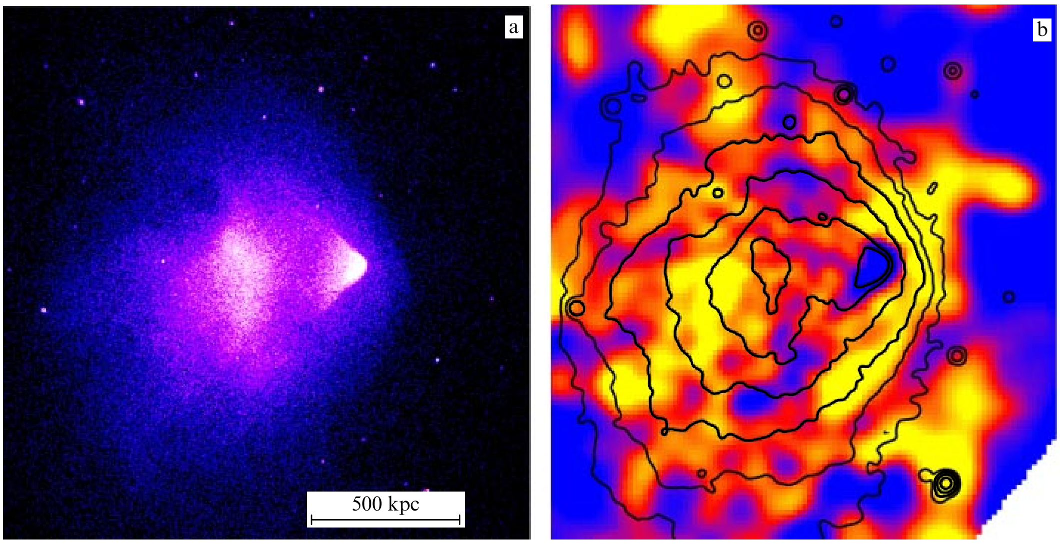

Figure 15. (Color online.) The merging cluster 1E0657-56. (a) The X-ray image and (b) gas temperature map obtained by Chandra [173–175]. Contours in panel b correspond to the X-ray brightness in panel a; temperature scale from 5 keV (in blue) to 20 keV (in yellow). A bright cold bullet that flew through the big cluster in the westward direction is seen (to the right). A shock wave propagates ahead of the bullet (rightmost contour).

The kinetic energy of colliding massive clusters reaches 10^{65} ergs; in the total energy, these events are second only to the Big Bang. During the collision, lasting for about 10^9 years, a substantial part of this energy (10–20%, the fraction in the gas component) is dissipated in the intergalactic gas via shocks and turbulence; as a result, the gas is heated to a temperature corresponding to a deeper potential well of the new cluster.

At first glance, after a sufficiently long time, gas and dark matter in an isolated cluster must come to virial and hydrostatic equilibrium. But the actual physics is more complicated. In the center of the cluster, a galaxy with an active nucleus is frequently found, which significantly changes the energy balance in its central relatively cold region (see Section 5 for more details). We also know from radio observations that magnetic field strengths $B \sim 1-10\ \mu$G and a turbulent structure [155, 156], and ultra-relativistic particles with $\gamma \sim 10^3 - 10^4$ [157] are present in the intergalactic plasma. Presumably, a certain part of the kinetic energy of colliding clusters is spent to enhancing the magnetic field and to accelerating particles in the cluster plasma.

These processes have been poorly explored, but numerical modeling and some observations suggest that the energy density of turbulence, magnetic fields, and relativistic particles can be of the same order of magnitude (see, e.g., [158, 159]), and must generally be much smaller than the thermal pressure.

In Sections 2 and 3, we considered the use of galaxy clusters, especially their mass functions at different epochs, for determining cosmological model parameters [76, 160] (see also the recent results in [147]). The accuracy of determining the mass is critically important for these experiments. However, the total cluster mass, dominated by invisible dark matter, is not measured directly but is obtained using indirect methods, for example, the hydrostatic equilibrium method [161], with the total mass estimated from the gas density and pressure gradients observed in X-rays, under the assumption that this gas is at rest and in equilibrium with the gravitational potential of the cluster. So far, such estimates have been sufficient, because the accuracy of the results have been limited by sparse cluster samples. In the nearest future, the sample sizes will dramatically increase (for example, the SRG observatory is expected to discover $\sim 10^4 - 10^5$ new clusters suitable for cosmological tests), which will require measuring the cluster mass with an accuracy of several percent. This accuracy cannot be achieved without the understanding (and appropriate numerical modeling) of the physics the intergalactic plasma. This includes, in particular, answering the following questions: How fast does the turbulence decay? What is the contribution of nonthermal effects to the energy balance of clusters? Do the plasma properties measured in the X-ray and microwave range correspond to real thermodynamic plasma properties?

Shock waves in clusters afford a promising instrument to probe the intergalactic plasma properties, to study clusters as a whole, and even to investigate some properties of dark matter. The launch of the Chandra observatory enabled X-ray studies of shock waves in the form of sharp density and temperature jumps in the gas. Shock waves have turned out to be a quite rare phenomenon: during more than 10 years of operation of the Chandra, XMM-Newton, and Suzaku satellites, only about a dozen have been discovered [162–171]. The gas pressure jump can also be observed in the microwave band via the SZ effect. In this way, the Planck observatory has already discovered two shock waves in the Coma cluster [172].

The first shock wave was discovered in the cluster 1E0657-56 (Bullet), shown in Fig. 15 [162, 173]. A brief inspection of the X-ray image reveals that two clusters are merging here, one of which (the relatively cold and dense gas 'bullet') has just flown through the massive cluster, and is currently flying from it and pushing a forward bow shock.

Figure 16 presents a numerical model for this cluster [176], with the total mass contours of two model clusters. The total mass map of 1E0657-56 is known from gravitational lensing [177, 178].

Figure 17 shows the X-ray brightness and projected gas temperature profiles inferred from Chandra observations, in a narrow sector passing through the head of the bullet and the shock. At the bullet boundary, the gas pressure is approxi-

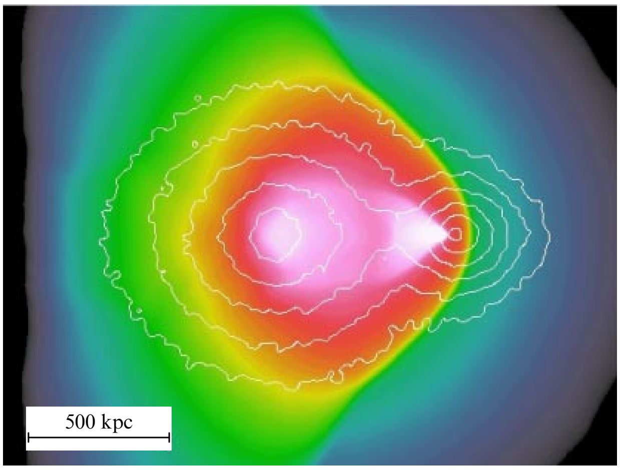

Figure 16. (Color online.) A numerical model of the cluster 1E0657-56 [176]. Colors indicate the X-ray brightness of the gas, contours show the total mass distribution (two clusters with different masses flew through each other in the sky plane). The model qualitatively reproduces the observations presented in Fig. 15.

mately constant (the gas density increases, but its temperature decreases). This contact discontinuity, or 'cold front' [179], is another interesting phenomenon in the intergalactic gas discovered by Chandra (which we do not discuss here). At the shock front, both the density and temperature increase, in agreement with the Hugoniot adiabat. The X-ray brightness profile is well described by the projection of the gas density jump by a factor of about three, which for an ideal gas corresponds to the Mach number 3.0 ± 0.4 [173]. Larger Mach numbers are not expected because the gas is in equilibrium with the gravitational potential, and the sound velocity inside it is of the order of the galactic radial velocity dispersion $\sigma_{\rm r}$. The depth of the potential at the cluster center is $\Phi_0 \approx -9\sigma_{\rm r}^2$, and the velocity of a test particle falling into such a potential well reaches the value corresponding to the Mach number $M \sim 3$. Indeed, all other known shocks in clusters have $M < 3$.

The velocity of the shock wave with $M = 3$ in 1E0657-56 is 4700 km s^{-1}. As follows from numerical simulations [176], the velocity of the bullet relative to the barycenter of the formed cluster is lower (≈ 2300 km s^{-1}); the difference is explained by the gas flow before the shock wave, which is induced by the gravitational attraction of the infalling bullet (its gravity advances hydrodynamic effects). For the same reason, the observed angle of the 'Mach cone' is substantially larger than expected in a homogeneous static medium: $\varphi = \arcsin M^{-1} = 20°$.

4.1 Bullet cluster and dark matter properties

From X-ray data, we derive the geometry and collision velocity of two clusters forming 1E0657-56. From the gravitational lensing, we can also reconstruct the total mass map [178], and from optical observations, we can reconstruct the mass distribution in galaxies.

In Fig. 18, an X-ray image and a total mass map are superimposed on the optical image of the cluster. As follows from optical spectra, the difference between radial velocities of the two galaxy clusters forming 1E0657-56 [181] is much smaller than the sky-projected velocity of the shock and the bullet. This supports the qualitative conclusion that the collision occurs almost in the plane of the sky, which can be inferred from the sharpness of the cold front and shock in the X-ray image. Moreover, the form of the shock and bullet suggests that the clusters collided head-on and the gas distribution is very likely to be axially symmetric. Based on these data, several interesting conclusions about dark matter can be inferred.

First, Fig. 18 directly confirms that dark matter really exists. Gas in clusters, including 1E0657-56, is the dominating visible matter component: its mass much exceeds that of galaxies. If there were no dark matter and the high velocity dispersion of galaxies (and the high gas temperature in clusters) were explained not by dark matter but, for exam-

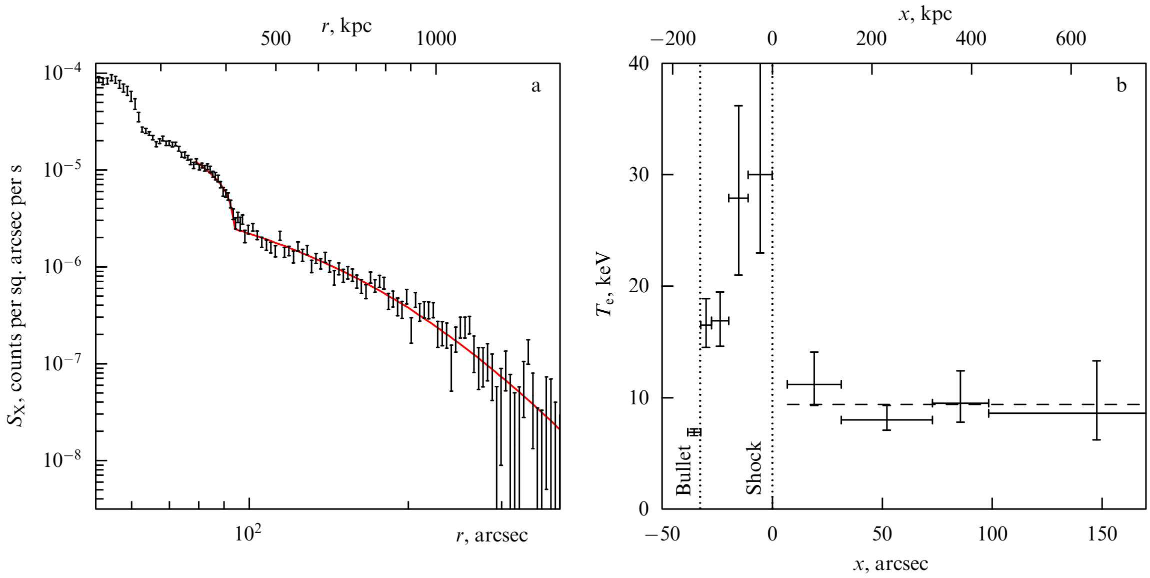

Figure 17. (Color online.) X-ray brightness profiles and projected temperature profiles for the cluster 1E0657-56 in a narrow sector passing through the bullet boundary and the shock wave (Chandra observations [173]). (a) The shock brightness profile is well described by a model with a sharp threefold gas density jump that has the shape of a spherical segment (the red line), as expected for the shock wave. (b) The vertical lines show the bullet boundary and the shock wave; the dashed horizontal line indicates the mean gas temperature ahead of the shock wave.

Figure 18. (Color online.) Maps of X-ray brightness (in pink; data from Fig. 15a) and of the total mass inferred from gravitational lensing (in blue, [178]), superimposed on the optical image of the cluster 1E0657-56. The X-ray gas is the dominant component of visible mater, but the total mass peaks lie outside the gas distribution peaks (and coincide with galaxy distribution peaks). This directly proves the existence of the dark matter component in clusters [177, 178] and points to its collisionless nature [180]. (Figure prepared by the press group of the Chandra observatory.)

ple, by modified gravity at large linear scales [182, 183], the gravitational lensing would indicate the total mass peaks of two clusters coincident with gas mass peaks. But this is not so (see Fig. 18): the total mass peaks are significantly offset from the visible mass peaks [177, 178]. This can only be explained by the presence of invisible matter with a mass several times higher than that of gas. Dark matter and gas are tightly linked by gravity and appear spatially separated only during cluster collisions; cluster 1E0657-56 is observed exactly in this rare stage. After these results were published, several other clusters with a similar spatial separation of the dark and visible components were reported [184–186], which rules out the possibility of explaining these observations in the framework of modified gravity theories by some rare geometric coincidences.

Next, as can be seen from Fig. 18, dark matter peaks coincide with peaks of the distribution of *collisionless* galaxies, which are clearly ahead of the gas along the collision trajectory. This offers the interesting opportunity to assess the validity of the common wisdom that dark matter is collisionless. Some observations may be better explained by assuming a nonzero cross section for dark matter particle self-interactions (see, e.g., [187]).

Hypothetical elastic collisions of dark matter particles would have several observable effects. For high collisional cross sections, dark matter would behave like a gas, which is obviously excluded by Fig. 18. Smaller cross sections would lead to finer effects, for example, to an anomalously low total-mass-to-light ratio for two cores of clusters after their passing through each other (which arises due to the scattering of dark matter particles, but not galaxies, outside cluster cores) and to a relative shift in the galaxy and dark matter distributions. No such effects are observed in the Bullet cluster. Using this fact, in [180, 188], an upper bound was derived for the elastic isotropic scattering cross section of dark matter particles as $\sigma/m < 0.7\ \mathrm{cm}^2\ \mathrm{g}^{-1}$ (where m is the unknown dark matter particle mass). Hence, almost the entire proposed interesting cross-section range (0.5–$5.0\ \mathrm{cm}^2\ \mathrm{g}^{-1}$) is ruled out. Observations of other similar clusters are consistent with this bound [184, 189] (the result reported in [190] for cluster A520, which was in contradiction with this upper bound, has not been confirmed by more precise data [186]).

This method for estimating σ/m is simple and relatively independent of the mass distribution details, but its accuracy is limited by the knowledge of the trajectory of clusters moving through each other. In the case of the Bullet cluster, the collision geometry is simple and obvious, which is not the case with other similar clusters, and therefore further improvement in the upper bounds for scattering cross sections by this method seems to be unlikely. A more sensitive method, based on the ellipticity of the cluster gravitational potential peak, was proposed in [191]; however, it is much more dependent on the accuracy of the dark matter profile measurement in the cluster core.

4.2 Electron–proton temperature equilibration in hot plasma

When a shock wave propagates through a fully ionized plasma, protons must be heated dissipatively and electrons must be compressed adiabatically (at least for sound Mach numbers $M \ll (m_{\mathrm{p}}/m_{\mathrm{e}})^{1/2} \approx 43$, which is well satisfied in the cluster plasma) and then heated (and protons cooled), due to the electron–proton heat exchange, to the average temperature prescribed by the Rankine–Hugoniot jump conditions. If the heat exchange occurs due to Coulomb collisions, the characteristic time of equating the electron (T_{e}) and proton (T_{p}) temperatures is [192, 193]

$$\tau_{\mathrm{C}} = 2 \times 10^8 \left(\frac{n_{\mathrm{e}}}{10^{-3}\ \mathrm{cm}^{-3}}\right)^{-1} \left(\frac{T_{\mathrm{e}}}{10^8\ \mathrm{K}}\right)^{3/2} [\mathrm{yr}]\,. \tag{6}$$

Besides Coulomb collisions, there can be other heat exchange mechanisms in a hot plasma with magnetic fields; therefore, the characteristic time τ_{C} is of great interest. Behind a shock wave propagating in plasma is a region where T_{e} has not yet reached the equilibrium value. Unequal T_{e} and T_{p} are expected in various astrophysical plasmas, such as the solar wind, supernova remnants, and the intergalactic medium outside the clusters. In these objects, it is very difficult to directly measure the time of the electron–ion heat exchange, because it is usually impossible to simultaneously measure T_{e} and T_{p} (and their variation) on scales where equilibrium can be reached (for example, in the solar wind plasma, this linear scale is about several astronomical units, and for supernova remnants, the time τ_{C} is comparable to their age).

In clusters, on the other hand, by a lucky coincidence, the gas parameters and linear scales are such that nonequilibrium regions are small compared to the cluster size and simultaneously can be resolved by telescopes. For example, in 1E0657-56, the width of such a region for the Coulomb equilibration timescale is 230 kpc, or $50''$, which is easily resolved by Chandra.

The T_{e} map in clusters can be constructed from X-ray spectra, while T_{p} cannot be directly measured yet. However, unlike shocks in supernova remnants, shocks in clusters are relatively weak, and their density jumps are sufficiently far from the asymptotic value for strong shocks ($\rho_1/\rho_0 = 4$ in a monoatomic gas). This allows using the density jumps, easily measured in X-ray plasma, to determine the Mach numbers and, correspondingly, the value of T_{p} immediately behind the shocks. This provides us with all necessary instruments to estimate the time the electron–ion equilibrium is established in the cluster plasma.

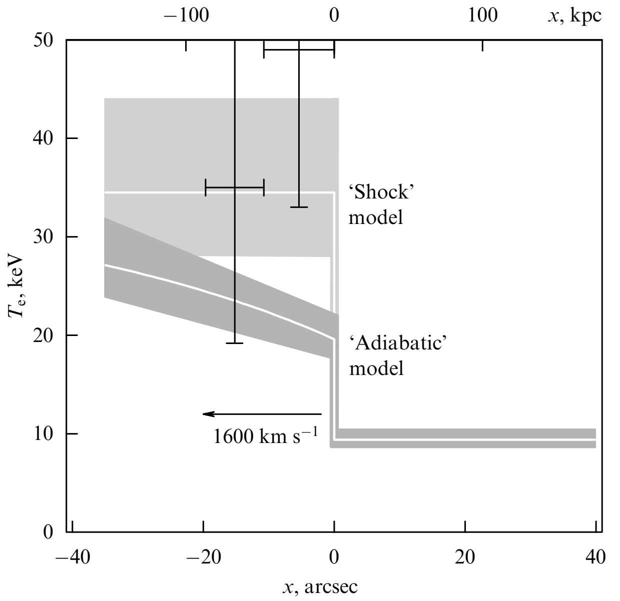

Figure 19. Three-dimensional (deprojected) electron temperature immediately behind the shock in 1E0657-56 [173]. Gray bands show predictions of two models. The 'adiabatic' model assumes the classical picture in which protons are heated by the shock and electrons are compressed adiabatically and then heated due to Coulomb collisions with protons. The 'shock' model assumes the instant heating of electrons in the shock to the mean gas temperature. The gas velocity in the shock reference frame (shown by the arrow) is calculated from the X-ray data.

Such measurements were conducted for 1E0657-56 [173, 179]. Figure 19 shows two models of the electron temperature profile formation across the shock: one model assumes adiabatic electron compression and subsequent heat exchange with $\tau = \tau_C$, and the other assumes their instant heating with $\tau \ll \tau_C$. The plasma velocity relative to the shock can be exactly derived from the temperature (and, correspondingly, the sound velocity) in front of the shock and the density jump at the shock. The measured values of T_e immediately behind the shock better agree with the model with $\tau \ll \tau_C$, although the measurement errors are high.

Similar measurements were carried out for two shocks in the cluster A2146 [165]. The results for them are not fully consistent with each other or with the results for 1E0657-56, and therefore the question on the rate of heat exchange in the cluster plasma remains open. We note that the Mach numbers in A2146 (2.3 and 1.6) are lower than in 1E0657-56 (3.0), and the difference between the adiabatic and dissipative heating is small and hence difficult to measure.

4.3 Constraints on diffusion in plasma

As noted in [165], the width of plasma density jumps in two shocks in A2146 is smaller than the mean free path of electrons, whereas the collisional diffusion would smear out the shock on a scale of a few mean free paths. This suggests that the diffusion is suppressed in the plasma. (Similar measurements of the shock in 1E0657-56 did not rule out both the zero front width and a smooth front [179].)

Interestingly, a similar observation was made for the density jump on the 'cold front' in A3667: the front is not resolved by Chandra, and its widening on the scale of several mean free paths is excluded with high confidence [179, 194]. The conclusion was the same: the diffusion is suppressed. However, a cold front (the contact discontinuity at the boundary of a moving gas cloud) and a shock are expected to have qualitatively different magnetic field structures: the field must drape around the cold front by forming a magnetic insulation layer [179, 195], and in the case of a shock, such insulation is not expected. Therefore, the absence of diffusion across the shock may suggest the suppression of diffusion in clusters in general.

A precursor of the electron temperature jump before the shock front is another expected manifestation of the electron diffusion through the shock [193, 196]. Unfortunately, even for such a well-measured cluster as 1E0657-56, the accuracy of data is insufficient to detect the precursor.

4.4 Ultrarelativistic electrons in the intergalactic plasma

As mentioned above, in addition to hot plasma, clusters contain magnetic fields and ultrarelativistic particles, from which synchrotron radio emission is observed [157]. Such electrons must, in addition, upscatter the CMB photons to X-ray frequencies. This inverse Compton scattering has not been discovered so far [197, 198], which is consistent with estimates of the mean magnetic fields in clusters $B > 1$ μG (for a given synchrotron brightness, the stronger the magnetic field is, the weaker the expected X-ray emission). Relativistic protons, which should accompany these electrons, have not been discovered yet either [199].

Although the existence of giant synchrotron radio halos covering the entire cluster and of peripheral arc-like 'relics' with sizes up to 1 Mpc has been recognized for a long time, the beginning of operation of new sensitive low-frequency telescopes — GMRT (Giant Meter-wave Radio Telescope), the upgraded VLA (Very Large Array), and LOFAR (Low-Frequency Array) — opened the new interesting field of cluster research. For halos and relics, it became possible to obtain brightness maps, their spectra, and their polarization with an angular resolution approaching that of X-ray observations, which resulted in a number of interesting findings.

The origin of relativistic electrons generating the radio halo is not completely clear [200]. The radiation cooling time of electrons with $\gamma \sim 10^4$ is $t_{\rm cool} < 10^8$ years, which is much shorter than their diffusion time through the cluster; therefore, they cannot be generated by the central radio galaxy and must be produced in situ. Giant radio halos are found exclusively in merging clusters [201]. In such clusters, shocks are expected that can accelerate electrons via the Fermi-I mechanism [202]. However, the shock velocities and $t_{\rm cool}$ are such that sources more similar to long and narrow periphery relics than to giant halos should arise. Indeed, for a long time shocks have been proposed to be responsible for the relics.

For example, in Fig. 20, shown are the spectral index and polarization maps of a well-studied radio relic, which are consistent with the expected electron cooling rate behind the shock and the expected magnetic field structure. The source is located at the expected periphery of the cluster CIZA2242 + 53 (Fig. 21), exactly where the shock is expected. In this case, the sensitivity of X-ray instruments was insufficient to detect the density jump and to confirm the presence of the shock [204], although a temperature jump was observed [169].

In two other cases, A521 (Fig. 22a) [170, 171] and A754 [166], shocks with $M = 2.4$ and $M = 1.6$ are visibly associated with radio relics. The radio spectra of both relics are well measured, and their steep slopes in both cases are consistent

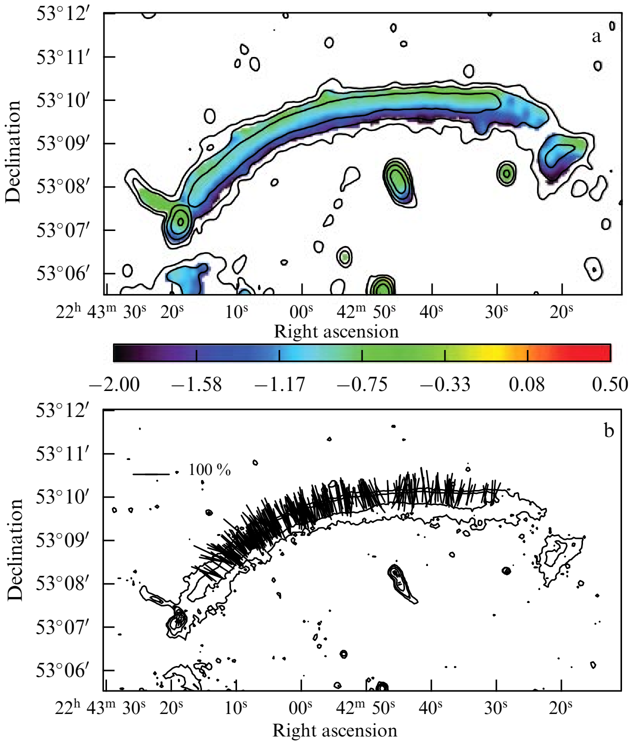

Figure 20. (Color online.) Spectral index and polarization (E vector) maps in the relic CIZA2242 + 53 [203]. (a) The spectral index change and (b) the polarization direction as a function of the distance from the edge of the relic qualitatively agree with those expected in the electron shock acceleration model and the chaotic magnetic field 'compressed' by the shock.

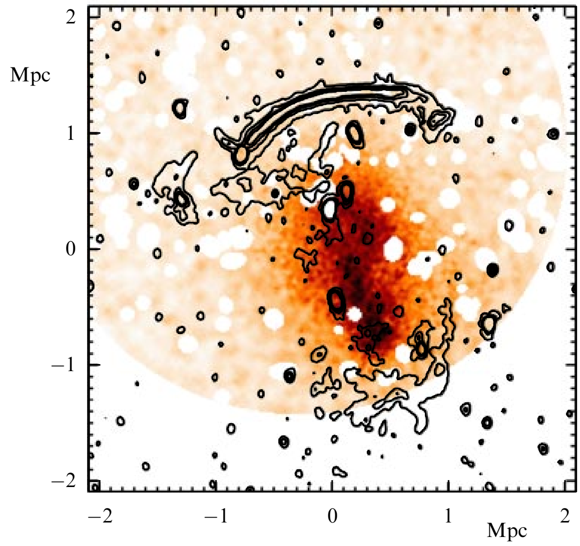

Figure 21. Radio relic in the cluster CIZA2242 + 53: radio brightness contours [204] superimposed on the X-ray image. The relic is located at the cluster periphery in the direction of its merging, where the shock can be expected.

with the expected spectral slope in the Fermi acceleration model for the Mach numbers derived from X-ray observations. (In several other clusters, the Mach numbers derived from X-ray and radio observations are different; see, e.g., [169, 208]. In those cases, shocks are not clearly seen in X-ray images, and the X-ray estimates are therefore questionable.) The coincidence of the relic locations with those shocks is quite unexpected: shocks with such low Mach numbers should have very low electron acceleration efficiency [209]. Moreover, as pointed out in [166], the extrapolation of the observed power-law spectrum of electrons with $\gamma \sim 10^3 - 10^4$ down to thermal energies predicts that the pressure of relativistic electrons must be comparable to the thermal pressure, which is inconsistent with observations. Therefore, the model with shock acceleration of electrons directly from the thermal reservoir is inapplicable here.

A more likely model seems to be the 're-acceleration' of relativistic electrons with $\gamma \sim 10^2$ (which live longer and can be accumulated in clusters [210]) by the same Fermi I mechanism. For a given Mach number, this mechanism provides the same power law slope of electrons at radio frequencies, and no problems with the acceleration efficiency and thermal pressure arise here [163, 211, 212].

As noted above, the shock acceleration cannot explain giant radio halos; another mechanism should be invoked. The most plausible one appears to be the Fermi II acceleration on turbulence that arises in the course of cluster merging. Of all particle acceleration mechanisms, this is the least effective one: it is incapable of sufficiently rapidly accelerating electrons from the thermal reservoir and hence also requires

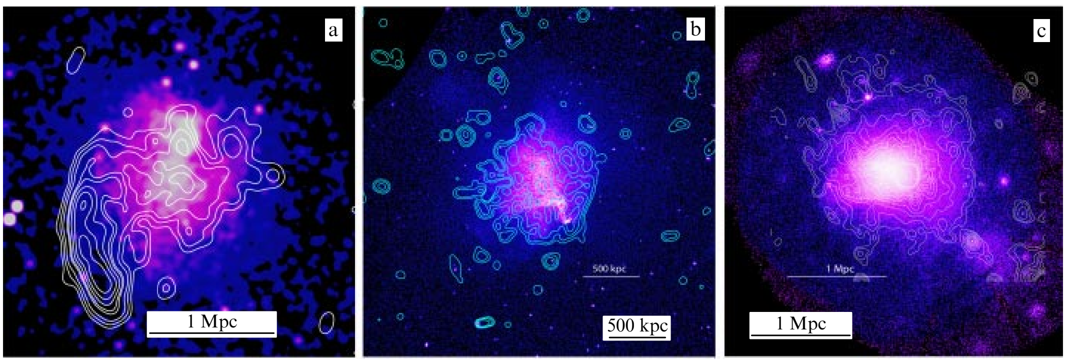

Figure 22. Examples of clusters with shocks that coincide by the position with periphery radio relics or with the sharp edge of a giant radio halo. The radio brightness contours are superimposed with the X-ray image. (a) A521 (GMRT, 240 MHz) [205]: the relic at the eastern edge of the cluster coincides with the shock [170, 171]. (b) A520 (VLA, 1.4 GHz) [206]: the sharp edge of the radio halo (south-west from the center) coincides with the shock seen in Fig. 14b [163]. (c) Coma (WSRT (Westerbork Synthesis Radio Telescope), 352 MHz) [207]: the sharp western edge of the halo coincides with the shock discovered by the Planck observatory [172].

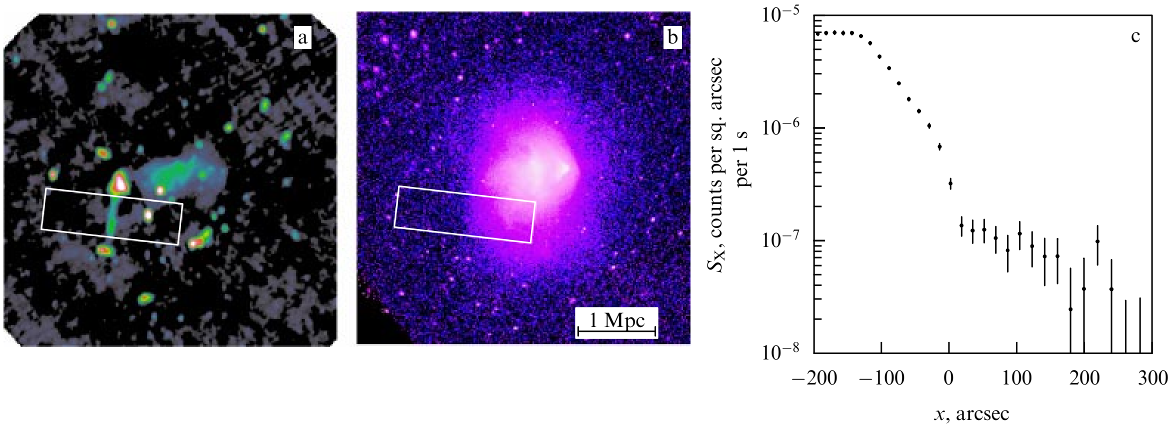

Figure 23. (Color online.) The probable second shock in the cluster 1E0657-56, as suggested by the presence of a radio relic [214]. (a) ATCA (Australian Telescope Compact Array) radio image showing a radio halo and a peripheral relic (crosses the rectangle near the center). (b) X-ray Chandra image (the same as in Fig. 15a, but with coloring that highlights the cluster periphery). A sharp X-ray brightness jump is observed near the relic. (c) X-ray brightness profile along the long side of the rectangle shown in panels a and b. The jump has the form characteristic for a gas density discontinuity in projection, and, apparently, is a shock.

aged relativistic electrons with $\gamma \sim 10^2$ as seed particles [200, 213]. We note that if such aged electrons, which cooled out of the radio band, are indeed ubiquitous in clusters, all periphery radio relics should be caused by shocks and all shocks would produce something similar to radio relics. This indeed seems to be observed, with a few exceptions likely explained by insufficient data sensitivity. For example, a second shock has recently been discovered in the Bullet cluster at the radio relic site (Fig. 23) [214]; the shock front in A521 (Fig. 22a) was discovered similarly [170]. At the same time, the locations of X-ray shocks in radio-halo clusters such as A520, Bullet, and Coma coincide with the sharp brightness edges of their radio halos (see Fig. 22).

Most likely, the radio halo and its sharp edge, spatially coincident with the shock, are physically different phenomena, which are related only by the geometry of the plasma flow during cluster collisions. Indeed, the radio halo edge frequently shows a spectrum that differs greatly from that of the main halo, being either steeper (A754) or flatter (A521), and at certain radio frequencies appearing like a separate peripheral relic.

4.5 Nearest prospects of cluster shock studies

As can be seen from the foregoing, this relatively new field of cluster studies is so far at a qualitative level, mainly due to the complexity of theoretical treatment and numerical simulations of nonthermal processes in turbulent magnetized plasmas. However, observations are progressing rapidly and are starting to attract the attention of plasma physics theorists. In the nearest future, X-ray data combined with low-frequency radio data could provide valuable information on microphysical properties of the intergalactic plasma.

The rapid progress in microwave instruments with high angular resolution and sensitivity is approaching the possibility of shock studies using the SZ effect. The ALMA (Atacama Large Millimeter/submillimeter Array) and GISMO (Goddard-Iram Superconducting 2-Millimeter Observer) instruments already are, and MUSTANG-2 (Multiplexed SQUID TES (Transition Edge Sensor) Array in Ninety GHz 2) will in the nearest future be capable of measuring the shock pressure jumps in clusters 1E0657-56, A520, and A2146. In the nearby clusters Coma, A3667, and A754, such measurements are accessible, in principle, to the Planck observatory.

The combination of X-ray and microwave observations allows eliminating the main source of uncertainty of shock parameters, the unknown geometry along the line of sight (similarly to determining the distance to the cluster in the well-known cosmological test). Currently, this uncertainty systematically constrains the accuracy of the limits of the electron–proton heat exchange rate [165].

5. Supermassive black holes in cluster centers

5.1 General picture

Unlike dark matter, the hot gas filling the entire volume of a cluster can radiate energy and cool. This process significantly complicates numerical modeling of the clusters and decreases the measurement accuracy needed for successful numerical simulations (see Section 2) and cosmological applications (Section 3) of clusters.

A 'surgical' way of accounting for cooling in the numerical data is to disregard the central zone of clusters and to use for analysis only the cluster outskirts, where the cooling time is long and apparently the role of the cooling is insignificant.

In the cluster centers, the situation is just the opposite: the radiation cooling time of the hot galactic gas ($\sim 10^9$ years) is much shorter than the age of the Universe. Without external energy sources, the gas should cool at a rate of $(10^2 - 10^3) M_\odot$ yr^{-1}. This is revealed by numerical simulations that take radiative losses of the gas into account. The cooling gas is turned into stars to form the central galaxy with a huge stellar mass an order of magnitude larger than the actual galactic masses.

However, X-ray and radio observations of nearby clusters show that the mechanical energy produced by the central supermassive black hole regulates the thermal balance of the gas and prevents it from uncontrolled cooling. Relativistic plasma flows inflate bubbles in the hot gas, which are lifted by the Archimedes force in the cluster atmosphere and transfer their energy to the gas. The efficiency of energy transfer from the bubbles to gas only weakly depends on the gas properties and turns out to be close to unity.

Simple arguments allow estimating the mechanical energy flux from the supermassive black hole based on the bubble size. This flux turns out to be equal to the gas radiative cooling losses by an order of magnitude in objects with a luminosity difference of more than 10^4 times. This suggests the presence of a feedback mechanism in the gas–black-hole system. With insufficient heating, the gas cooling increases the accretion rate onto the black hole and hence increases the mechanical energy flux and gas heating.

Such processes, observed in nearby galaxy clusters, can regulate both the black-hole growth rate and the star formation rate in forming elliptical galaxies at $z \sim 2-3$. The key factor determining the transformation of the rapid black hole growth and active star formation into the passive stage is the high efficiency of gas heating by the mechanical energy fluxes compared to the radiative heating. This provides the heating and cooling balance even for comparatively low gas accretion rates.

Below, we consider only very general issues of the central black hole mass activity effects on the cluster gas. For a more detailed discussion, see, e.g., reviews [215, 216].

5.2 Gas cooling

The radiative cooling time of a hot rarefied gas in the galaxy cluster cores,

$$t_{\text{cool}} = \frac{\gamma}{\gamma - 1} \frac{n k_{\text{B}} T}{n^2 \Lambda(T)} \lesssim 10^8 - 10^9 \text{ years},$$

is much shorter than the Hubble time (see, e.g., [217–219]). Here, n and T are the density and temperature of the gas, γ is the adiabatic index, and $\Lambda(T)$ is the cooling function.

In the absence of an external energy source, a cooling gas flow toward the cluster center should arise (see, e.g., a description of this scenario in review [220]). However, the high rate of gas cooling,

$$\dot{M}_{\text{cool}} = \frac{L_{\text{cool}}}{[\gamma/(\gamma - 1)] k_{\text{B}} T} \mu m_{\text{p}} \sim (10^2 - 10^3) M_{\odot} \, [\text{yr}^{-1}],$$

contradicts observations (see, e.g., [221]) by an order of magnitude at least. Here, $L_{\text{cool}} \approx L_{\text{X}}$ is the total luminosity of the gas and μ is the mean atomic weight of gas particles.

To solve this contradiction, a powerful external source of gas heating is needed. In the late 1990s and early 2000s, it became clear that the central supermassive black hole can be such a source.

5.3 Observational appearances of the interaction of gas and a supermassive black hole

Giant elliptical galaxies with supermassive black holes ($M_{\text{BH}} \gtrsim 10^9 \, M_{\odot}$) reside in the centers of regular galaxy clusters. Such a black hole, accreting matter at a rate close to the Eddington value, is able to radiate a power of up to 10^{47} erg s^{-1}, more than enough to compensate the radiative cooling losses of the gas.

However, such bright sources have never been observed in nearby clusters. In addition, the efficiency of the radiative energy transfer to a fully ionized gas (via Compton heating) is low. At the same time, radio observations of the synchrotron emission from the relativistic plasma of jets and the analysis of the particle acceleration efficiency suggest that the jet mechanical energy greatly exceeds the observed black hole luminosity in the central galaxy of the brightest X-ray cluster in Perseus (see, e.g., [222]). The mechanical energy of black holes was taken into account in theoretical models of individual elliptical galaxies [223, 224]. However, to the full extent, the black hole impact was revealed by comparing X-ray and radio observations of nearby galaxy clusters.

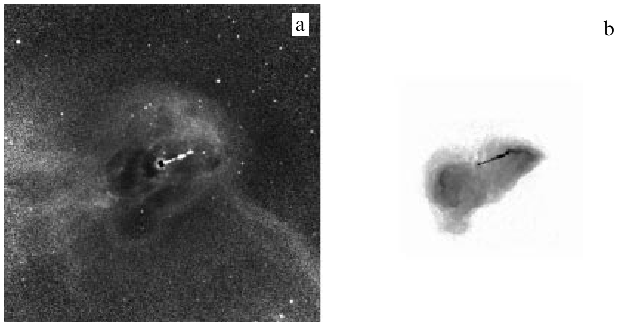

Figure 24. (a) X-ray [230] and (b) radio (wavelength 6 cm) [235] images of the central region ($3' \times 3'$) of galaxy M87. Bubbles of relativistic plasma (panel b), inflated by the central supermassive black hole, push out the thermal plasma to form the low-brightness regions seen in the X-ray image (panel a).

The first compelling evidence of the interaction of relativistic plasma flows from supermassive black holes with hot gas was deduced from X-ray images of the central parts of the Perseus cluster (Abell-426) and M87 galaxy (the central galaxy of the Virgo cluster) obtained by the ROSAT satellite [225, 226]. Based on this data, the mechanical energy flux from supermassive black holes was directly estimated, and a simple physical model for gas heating was suggested [227, 228]. New observations with Chandra and XMM-Newton allowed extending this analysis to many dozens of objects (see, e.g., [229–234]).

Generally, the interaction of the black hole mechanical energy with gas is similar to processes occurring during powerful explosions in Earth's atmosphere, which are described, for example, in Zeldovich and Raizer's book [29]. The M87 galaxy in the Virgo cluster provides a compelling example. Figure 24 shows X-ray and radio images of M87 (central $3' \times 3'$). Synchrotron radiation from the relativistic jet is clearly seen in both images. At the same time, we observe a clear anticorrelation between the X-ray flux produced by thermal plasma with a temperature of 1–2 keV and the radio flux related to synchrotron emission of relativistic electrons. This means that relativistic plasma bubbles inflated by the supermassive black hole push out the thermal plasma. In the model where a constant energy injection L_M by the supermassive black hole is assumed, the initial phase of the bubble expansion is supersonic, and its radius increases as $r \propto t^{3/5}$. As the bubble expands, its expansion velocity becomes subsonic. Because we do not see any signatures of a powerful shock in the surrounding gas, it is this stage that is currently observed in the M87 galaxy nucleus. The minimal energy required to create such a bubble is determined by its enthalpy,

$$E_{\text{bubble}} = \frac{\gamma}{\gamma - 1} \, pV,$$

where γ is the adiabatic exponent inside the bubble ($\gamma = 4/3$ for the relativistic plasma), p is the pressure of the surrounding thermal plasma, and V is the bubble volume.

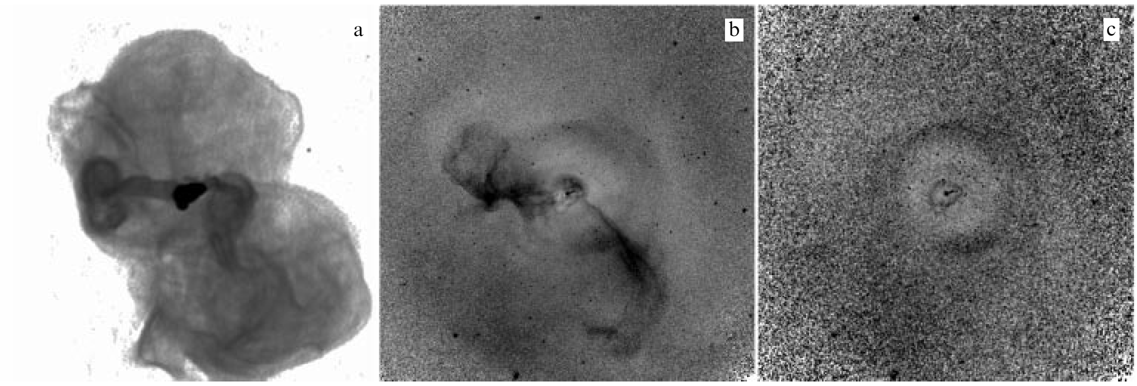

Figure 25. (a) Large-scale structure of M87 seen in the radio band (size $\sim 7' \times 7'$, wavelength 90 cm) [236]. Three generations of 'bubbles' are clearly visible: (1) the bubble in the central region immediately around the jets; (2) toroidal structures associated with the evolution of the bubbles as they rise in the atmosphere; (3) large regions on both sides of the core associated with the 'oldest' bubbles. (b) X-ray (0.5–3.5 keV) image of M87. Visible are filaments of the relatively cold ($T \lesssim 1$ keV) gas following the bubble. (c) X-ray (3.5–7.5 keV) image in which the observed X-ray flux reflects the gas pressure distribution, allowing the bright X-ray ring at a distance of $\sim 2.7'$ from the center to be interpreted in terms of a shock.

At the subsonic expansion stage, the Rayleigh–Taylor instability starts deforming the bubble, and the Archimedes force carries it outside the central region. To estimate the mechanical energy power, it is possible to use the estimate of the bubble lifetime due to the Archimedes force [227]. Indeed, the velocity of a bubble rising in a stratified thermal plasma atmosphere is determined by the balance between the Archimedes force and the gas drag:

$$g\,\frac{4}{3}\,\pi r^3 \rho_{\rm gas} \approx C\pi r^2 \rho_{\rm gas} v_{\rm rise}^2\,,$$

where g is the gravity acceleration, r is the bubble size, and C is a dimensionless constant of the order of unity (for a low-viscosity gas). Hence, $v_{\rm rise} \sim \sqrt{gr}$. On the other hand, the bubble expansion velocity is determined by the power L_M of the relativistic plasma flow that blows the bubble,

$$v_{\rm exp} \sim \frac{L_M}{4\pi r^2 p}\,,$$

(for subsonic expansion). The condition $v_{\rm exp} \gtrsim v_{\rm rise}$ means that the Archimedes force has no time to substantially shift the expanding bubble. Applied to bubbles in the inner region of M87 (see Fig. 24), this condition yields the mechanical power estimate $L_M \sim 10^{43}$ erg s^{-1}, which roughly corresponds to gas radiative losses. An equivalent estimate can be obtained by simply dividing the bubble energy by the time it rises a distance of the order of its radius, $t_{\rm bubble} \sim r/v_{\rm rise} \sim \sqrt{r/g}$. Of course, such estimates and their modifications (see, e.g., [215]) give only an order-of-magnitude value of L_M.

It can be expected that during the initial phase of bubble formation (when its radius is small), its expansion velocity is supersonic, and a shock wave starts propagating through the hot gas. When the expansion velocity becomes subsonic, the shock wave runs ahead. This wave allows independently estimating the total energy released by the supermassive black hole during bubble formation. A shock wave is clearly seen in M87 (Fig. 25) at a distance of $\sim 2.7'$ from the center [230, 237]. The temperature and density jumps at the shock front correspond to the Mach number $M \sim 1.2$. From simple one-dimensional calculations, we can estimate the total energy released, $E \sim 5 \times 10^{57}$ erg, and the time of bubble formation, ~ 12 mln years. The ratio of these quantities yields the mean energy power $L_M \sim 10^{43}$ erg s^{-1} over this period, which is also consistent with gas cooling energy losses. The fraction of the shock energy in this calculation is about 25% of the total energy: the other 75% turned into bubble enthalpy or was spent to heat the gas at the initial strong shock stage.

5.4 Mechanical energy dissipation

A rising relativistic plasma bubble can be transformed into a toroidal structure (Figs 25 and 26), reminiscent of the mushroom cloud arising from powerful atmospheric explosions. As in the case of explosions, the bubble entrains low-entropy gas, which cools in adiabatic expansion to form cold gas filaments following the mushroom (see, e.g, [228, 238, 239]).

The rising bubble travels with the speed $v_{\rm rise} \sim \sqrt{gr}$, which does not exceed the sound speed in the thermal plasma and is

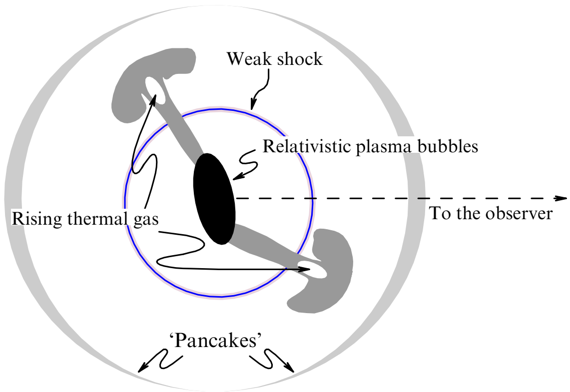

Figure 26. Schematic view of the interaction of relativistic plasma bubbles inflated by a supermassive black hole, as suggested by the analogy with processes occurring during strong atmospheric explosions. Relativistic plasma bubbles at the center are currently being formed by the relativistic plasma outflow from the black hole. The ring shows an expanding spherical (weak) shock caused by the bubble formation. The relativistic plasma bubble rising by the Archimedes force can be transformed into a toroidal structure, reminiscent of the mushroom cloud arising from powerful atmospheric explosions. As in the case of the explosions, the bubble entrains low-entropy gas, which cools in the course of the adiabatic expansion and forms filaments following the bubble. At late evolutionary stages, the bubbles turn into oblate (in radius) structures (see Fig. 25). (Figure adapted from [228].)

much lower than the sound speed in the relativistic plasma inside the bubble. As a result of the adiabatic expansion of matter inside the bubble, the energy (enthalpy) stored in the bubble decreases in correspondence with the decrease in the pressure of the ambient gas:

$$E = \frac{\gamma}{\gamma - 1}\, pV \propto p^{(\gamma-1)/\gamma}\,.$$

Therefore, the bubble, after having risen a distance of several pressure scale heights of the atmosphere, completely loses the stored energy, which is transferred to the surrounding gas. This energy is spent to overcome the gas drag, to generate internal waves and turbulence behind the bubble, etc. Details of these processes depend on the gas properties (in particular, on the viscosity) and the presence of magnetic fields. The subsonic character of bubble motion means that only a small fraction of the energy turns into sound waves. The energy transferred to the surrounding gas by other processes turns out to be 'bound' to the gas and ultimately is transformed into heat in the central zone of the cluster.

Thus, we can expect that a significant fraction of the black-hole mechanical energy is turned into gas heating, irrespective of the specific mechanism of energy transfer and dissipation. In fact, the central part of the cluster works like a calorimeter by intercepting almost all mechanical energy from the black hole [240].

A substantial fraction of the energy (several dozen percent) can be transformed into a quasi-spherical weak shock/sound wave (see Fig. 25) propagating through the cluster gas. Unlike dissipation in a strong shock, the energy dissipation in the sound wave depends on the gas properties (viscosity and heat conductivity). However, it is quite likely that such waves can dissipate most of their energy in the central zone of the cluster [241], leading to an additional gas heating. In this way, the energy is injected isotropically, making such a heating mechanism very attractive. However, it is not obvious that a fraction of energy exceeding $\sim 25\%$ can be transferred to the sound waves [237]. The dominant gas heating mechanism is probably the bubble's enthalpy dissipation and heating at the strong shock stage (if such a stage actually occurs).

5.5 Feedback mechanism

The signatures of the black hole mechanical energy effects on the surrounding gas are observed is systems that differ in size by several orders of magnitude, starting from dwarf elliptical galaxies, such as NGC5813 [242], and ending with massive clusters, such as MS0735.6+7421 at the redshift $z = 0.22$ [243]. The bubble volumes in these systems differ by about four orders of magnitude. Nevertheless, in each of these systems, the estimates of mechanical energy fluxes and gas cooling rates are comparable. A systematic comparison of the gas heating and cooling (see, e.g., [232, 233]) revealed a compelling correlation between these quantities for several dozen objects (Fig. 27).

Hence, the activity of a supermassive black hole can adjust to the gas cooling rate in every system. In fact, the gas–supermassive-black-hole system represents a self-regulating system with negative feedback. The general scheme is as follows: decreasing the energy release from the black hole leads to gas cooling; the gas starts flowing toward the cluster center, thus increasing the mass accretion rate onto the black hole and hence increasing the energy release.

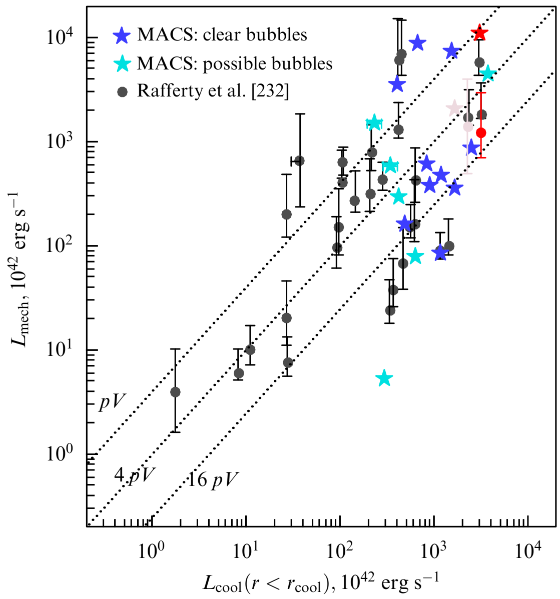

Figure 27. Comparison of the mechanical power of a supermassive black hole and cooling losses of the gas for a large cluster sample; p and V are the pressure and volume of the bubbles. Despite the large scatter, a correlation is evident. This correlation indicates that the black hole power is 'regulated' to provide approximate balance between heating and cooling. (From paper [233].)

We consider two simplest mechanisms providing such a feedback.

In the first (see, e.g., [240, 244]), accretion occurs directly from the hot gas, and its rate is described by the classical Bondi formula [245] for spherically symmetric adiabatic gas flow onto a central compact object, $\dot{M} \sim \pi (G M_{\rm BH})^2 c_{\rm s}^{-3} \rho$, where $c_{\rm s} = (\gamma k_{\rm B} T/(\mu m_{\rm p}))^{1/2}$ is the sound velocity in the gas and ρ is the gas density. In terms of gas parameters, the accretion rate is proportional to $n/c_{\rm s}^3 \propto n/T^{3/2} \propto s^{-3/2}$, where $s = T/n^{2/3}$, i.e., is in fact determined by the gas entropy.

We note that in a stable atmosphere, low-entropy gas accumulates at the bottom of the potential well, where the black hole resides. The accretion rate is therefore determined by the minimal gas entropy in the entire system. Such a system can establish the balance between gas heating and cooling.

Interestingly, estimates of the expected energy release in several nearby clusters, obtained using the Bondi formula, are in reasonable agreement with estimates derived from bubble sizes (see, e.g., [240, 244, 246]). Here, it should be borne in mind that due to the presence of angular momentum in the gas, the Bondi solution can hardly be applied near the black hole. In this model, it only determines the mass accretion rate at the capture radius.

In the second variant (see, e.g., [247, 248]), a small amount of gas has time to cool to form cold gas clouds. The clouds move in the potential well of the central part of the cluster, collide, and lose the angular momentum, and eventually supply material for accretion onto the supermassive black hole. This variant was conventionally called 'cold accretion', as opposed to the 'hot accretion' described by the Bondi formula.

The two variants described above strongly differ in the details of how the gas falls onto the black hole, but rely on the common assumption that insufficient gas heating leads to an

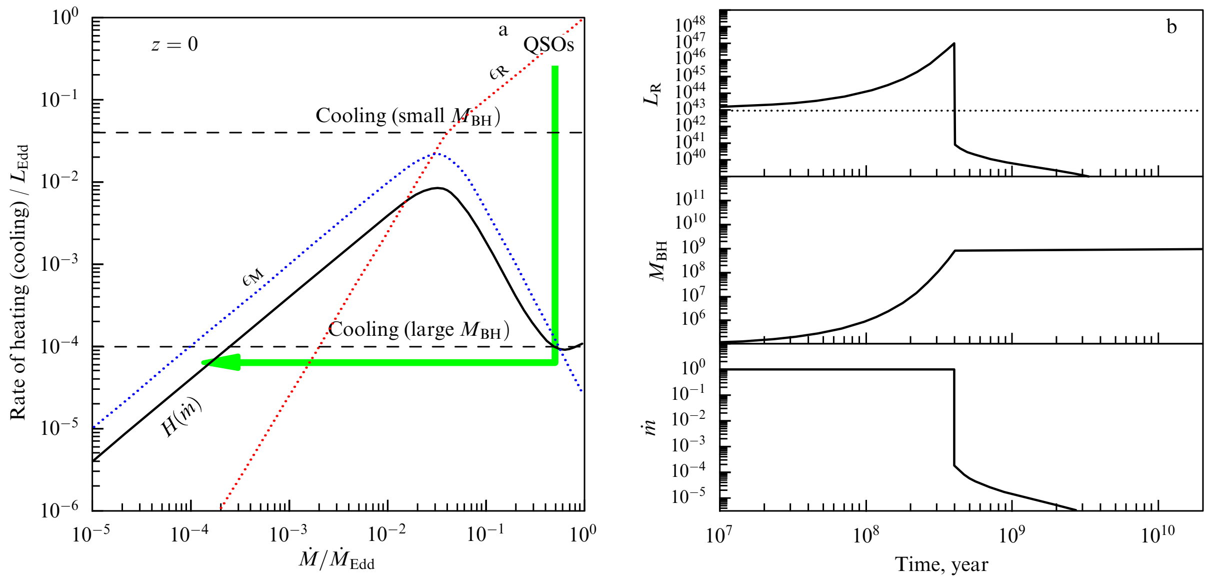

Figure 28. (a) Qualitative picture of a black hole and host galaxy evolution under the condition that the gas heating as a function of the accretion rate be described by Eqn (7). The dotted curves show the energy released as radiation and as mechanical energy (in units of the Eddington luminosity). The solid curve shows the total heating rate obtained with the efficiency of transformation of different forms of energy into gas heating (the coefficients α_M and α_R) taken into account. The heating rate turns out to be a nonmonotonic function of the accretion rate. The horizontal line shows the cooling losses of the gas. As the supermassive black hole mass increases, the horizontal line shifts downwards. The black hole transits from the high-accretion rate, high-luminosity quasar state (QSO, quasi-stellar object) into a state with low luminosity but with a sufficiently efficient gas heating due to the mechanical energy. The growth of the supermassive black hole mass drastically decreases, and the gas cooling and star formation stop. (b) Schematic representation of the evolution of the observed black hole characteristics. The bright quasar phase is followed by the radio source phase with a slow growth of the black-hole mass. (Figure adapted from paper [249].)

increase in the accretion rate onto the black hole and the accretion power.

5.6 Relation to the evolution of elliptical galaxies

Compelling evidence of the influence of supermassive black holes on gas cooling in nearby galaxy clusters suggests that a similar process may affect the formation and evolution of galaxies at $z \sim 2-3$. For this to be the case, three conditions must be satisfied: (1) the black hole mass must be sufficiently large; (2) a significant fraction of the black hole power must be in the mechanical form; (3) gas must form an extended quasispherical atmosphere.

The first condition simply allows the black hole to generate enough power to significantly affect the thermodynamic properties of gas on the galactic scale. The combination of the second and third conditions provides high efficiency of this energy reprocessing into gas heating.

In the framework of a simple qualitative model [249], the gas heating due to the black hole power accreting with a rate $\dot{M}$ can be written as

$$H(\dot{M}) = \big(\alpha_M \epsilon_M(\dot{m}) + \alpha_R \epsilon_R(\dot{m})\big) 0.1 \dot{M} c^2 \,, \qquad (7)$$

where $\dot{M}$ and $\dot{m}$ are the mass accretion rates in physical units and in units of the Eddington luminosity respectively, $\epsilon_M(\dot{m})$ and $\epsilon_R(\dot{m})$ characterize the efficiency of the accreting matter rest-mass energy transformation into mechanical energy and radiation, and the coefficients α_M and α_R are responsible for the conversion of these energy forms into gas heating. The typical value is $\alpha_R \sim 10^{-5} - 10^{-4} \ll 1$ [250, 251], whereas the value of α_M can be close to unity. This big difference between α_R and α_M is the key property of the model being discussed.

The values of $\epsilon_M(\dot{m})$ and $\epsilon_R(\dot{m})$ are determined by the accretion physics. We assume that at high accretion rates, the radiation production efficiency is high (for example, $\epsilon_R \sim 0.1$), but this efficiency decreases at lower accretion rates. By contrast, the mechanical energy production efficiency is high at low accretion rates and decreases at high accretion rates (Fig. 28). At a qualitative level, this follows from both theoretical accretion models (see, e.g., [252–254]), and from observations of X-ray binaries in our Galaxy (see, e.g., [255]) and active galactic nuclei (see, e.g., [236]). Considering the huge difference between α_M and α_R, such a dependence of $\epsilon_M(\dot{m})$ and $\epsilon_R(\dot{m})$ on the mass accretion rate implies that a given level of heating can be provided by two totally different accretion regimes [249]. In the first, the accretion rate is very high and the black hole luminosity is close to the Eddington value; however, with $\alpha_R \ll 1$, only a small fraction of this power is converted to gas heating. In the second regime, the accretion rate is low, and the heating is due to the higher value of α_M.

Schematically, the evolution of the system consisting of a black hole and gas in a galaxy is shown in Fig. 28. At the initial stage, insofar as the black hole mass is small, the system is in a state in which the gas rapidly cools and the black hole mass grows rapidly, with a large part of the black hole accretion power is spent to radiation. At later stages, the black hole switches to the regime with a low accretion rate, and most of the accretion power is released as mechanical energy (relativistic plasma flows), whereas the observed black hole luminosity decreases by several orders of magnitude. Here, due to the high heating efficiency by mechanical energy, the gas cooling stops, and the galaxy transits to the passive evolution stage without powerful star formation.

Of course, this is only a very rough description of processes that determine the joint evolution of black holes and the host galaxies. Numerical (semi-analytic) models (e.g., those in [256, 257]) indicate that scenarios based on the high gas heating efficiency by the black-hole mechanical power may provide a qualitative explanation of galaxy evolution, but many details of this process remain unclear. However, it is important that galaxy cluster research provides us with the unique possibility of investigating the physics of the interaction of black holes with the surrounding hot gas.

6. Conclusion

We have discussed only a few of the most important aspects of galaxy cluster studies, which were in the sphere of the scientific interests of Yakov Borisovich Zeldovich, from the large-scale structure of the Universe and cosmology to accretion onto black holes and gas dynamics.

Many issues remained beyond the scope of this review, but what we have said is already sufficient to appreciate the important role of galaxy clusters in modern astrophysics. In recent decades, the clusters have become a powerful tool in cosmological and plasma physics studies. They are observed with the best ground-based and space telescopes. Clusters have revealed the effects of supermassive black holes on the thermodynamics of the surrounding gas; the obtained conclusions were expanded to star formation process in galaxies in general. At the same time, vast computational resources are being allocated to model the formation and evolution of galaxy clusters. It suffices to say that the number of massive clusters 'born' in numerical simulations is several orders of magnitude larger than the total number of clusters in the observable part of the Universe.

Such is the current state of cluster astrophysics. The nearest future promises a qualitative leap forward in a number of directions. The Japanese X-ray observatory Astro-H[9] (thanks to cryogenic bolometers used as X-ray spectrographs with a resolution $E/\Delta E > 1000$) will be able to directly measure gas velocities in clusters, which will enable us to resolve many issues in plasma physics and to improve cluster mass measurements derived from the hydrostatic equilibrium equation. The SRG observatory (a joint Russian–German project) will be able to discover *all* massive clusters (with masses greater than $\sim 3 \times 10^{14} M_{\odot}$) in the observable Universe and provide cosmologists with the 'ultimate' cluster catalog for studying the dark energy equation of state. Simultaneously, cluster observations though the Sunyaev–Zeldovich effect with different instruments (the Planck satellite, APT, ACT, CARMA,[10] MUSTANG on GBT,[11] BOLOCAM on JCMT,[12] and ALMA) will allow independent (and jointly with SRG) studies of distant clusters and the gas physics inside them.

Already now, the ALMA telescope of the European Southern Observatory is conducting detailed observations of the cold gas in cluster centers and soon will be able to provide much new information on the complex physics of star-formation processes and effects from supermassive black holes. Massive optical surveys are underway, including the infrared survey of the WISE satellite (Wide-field Infrared Survey Explorer) and the newest radio sky surveys. Under development is the new generation of X-ray observatories, including Athena of the European Space Agency and SMART-X (Square Meter Arcsecond Resolution) in the USA.

Undoubtedly, cluster astrophysics is in for a flourishing period, in which ideas put forward by Yakov Borisovich Zeldovich continue to play a key role.

[9] http://astro-h.isas.jaxa.jp/en/.
[10] Combined Array for Research Millimeter-wave Astronomy.
[11] Green Bank Telescope.
[12] James Clerk Maxwell Telescope.

References

1. Zeldovich Ya B, Einasto J, Shandarin S F *Nature* **300** 407 (1982)
2. Gott J R (III) et al. *Astrophys. J.* **624** 463 (2005)
3. Ade P A R et al. (Planck Collab.) *Astron. Astrophys.*, submitted; arXiv:1303.5084
4. Dolgov A D, Sazhin M V, Zeldovich Ya B *Basics of Modern Cosmology* (Gif-sur-Yvette: Editions Frontières, 1990); Translated from Russian: Dolgov A D, Zeldovich Ya B, Sazhin M V *Kosmologiya Rannei Vselennoi* (Moscow: Izd. MGU, 1988)
5. Mukhanov V F, Feldman H A, Brandenberger R H *Phys. Rep.* **215** 203 (1992)
6. Starobinskii A A *JETP Lett.* **30** 682 (1979); *Pis'ma Zh. Eksp. Teor. Fiz.* **30** 719 (1979)
7. Starobinsky A A *Phys. Lett. B* **91** 99 (1980)
8. Guth A H *Phys. Rev. D* **23** 347 (1981)
9. Linde A D *Phys. Lett. B* **108** 389 (1982)
10. Albrecht A, Steinhardt P J *Phys. Rev. Lett.* **48** 1220 (1982)
11. Mukhanov V F, Chibisov G V *JETP Lett.* **33** 532 (1981); *Pis'ma Zh. Eksp. Teor. Fiz.* **33** 549 (1981)
12. Mukhanov V F, Chibisov G. *Sov. Phys. JETP* **56** 258 (1982); *Zh. Eksp. Teor. Fiz.* **83** 475 (1982)
13. Starobinsky A A *Phys. Lett. B* **117** 175 (1982)
14. Bardeen J M, Steinhardt P J, Turner M S *Phys. Rev. D* **28** 679 (1983)
15. Zeldovich Ya B *Mon. Not. R. Astron. Soc.* **160** 1P (1972)
16. Zel'dovich Ya B, Novikov I D *Sov. Astron.* **13** 754 (1970); *Astron. Zh.* **46** 960 (1969)
17. Harrison E R *Phys. Rev. D* **1** 2726 (1970)
18. Peebles P J E, Yu J T *Astrophys. J.* **162** 815 (1970)
19. Rubakov V A *JCAP* (09) 030 (2009)
20. Guth A H, Pi S-Y *Phys. Rev. Lett.* **49** 1110 (1982)
21. Ade P A R et al. (Planck Collab.) *Astron. Astrophys.*, submitted; arXiv:1303.5082
22. Hu W et al. *Phys. Rev. D* **57** 3290 (1998)
23. Seljak U et al. *Phys. Rev. D* **68** 083507 (2003)
24. Hinshaw G et al. *Astrophys. J. Suppl.* **208** 19 (2013)
25. Ade P A R et al. (Planck Collab.) *Astron. Astrophys.*, submitted; arXiv:1303.5076
26. Diemand J, Moore B, Stadel J *Nature* **433** 389 (2005)
27. Zel'dovich Ya B *Astrophysics* **6** 164 (1970); *Astrofiz.* **6** 319 (1970)
28. Zel'dovich Ya B *Astron. Astrophys.* **5** 84 (1970)
29. Zel'dovich Ya B, Raizer Yu P *Elements of Gasdynamics and the Classical Theory of Shock Waves* (New York: Academic Press, 1968); Translated from Russian: *Fizika Udarnykh Voln i Vysokotemperaturnykh Gidrodinamicheskikh Yavlenii* (Moscow: Nauka, 1966)
30. Doroshkevich A G *Astrophysics* **6** 320 (1970); *Astrofiz.* **6** 581 (1970)
31. Shandarin S F, Zeldovich Ya B *Rev. Mod. Phys.* **61** 185 (1989)
32. Yoshisato A et al. *Astrophys. J.* **637** 555 (2006)
33. Doroshkevich A G, Ryaben'kii V S, Shandarin S F *Astrophysics* **9** 144 (1973); *Astrofiz.* **9** 257 (1973)
34. Doroshkevich A G, Sunyaev R A, Zeldovich Ia B, in *Confrontation of Cosmological Theories with Observational Data. Proc. of the Symp., Krakow, Poland, September 10–12, 1973* (Proc. IAU Symp., Vol. 63, Ed. M S Longair) (Dordrecht: D. Reidel Publ. Co., 1974) p. 213
35. Doroshkevich A G, Shandarin S F *Sov. Astron.* **22** 653 (1978); *Astron. Zh.* **55** 1144 (1978)
36. Bond J R, Kofman L, Pogosyan D *Nature* **380** 603 (1996)
37. Shandarin S F, Sathyaprakash B S *Astrophys. J.* **467** L25 (1996)
38. Shandarin S F *JCAP* (02) 031 (2009)
39. Gurbatov S N, Saichev A I, Shandarin S F *Mon. Not. R. Astron. Soc.* **236** 385 (1989)
40. Kofman L et al. *Astrophys. J.* **393** 437 (1992)
41. Coles P, Melott A L, Shandarin S F *Mon. Not. R. Astron. Soc.* **260** 765 (1993)

42. Lee J, Shandarin S F *Astrophys. J.* **500** 14 (1998)
43. Doroshkevich A G et al. *Mon. Not. R. Astron. Soc.* **192** 321 (1980)
44. Klypin A A, Shandarin S F *Mon. Not. R. Astron. Soc.* **204** 891 (1983)
45. Efstathiou G et al. *Astrophys. J. Suppl.* **57** 241 (1985)
46. Crocce M, Pueblas S, Scoccimarro R *Mon. Not. R. Astron. Soc.* **373** 369 (2006)
47. Bryan G L et al. *Comput. Phys. Commun.* **89** 149 (1995)
48. Bryan G L et al. (The Enzo Collab.), arXiv:1307.2265
49. Kravtsov A V, Klypin A A, Khokhlov A M *Astrophys. J. Suppl.* **111** 73 (1997)
50. Teyssier R *Astron. Astrophys.* **385** 337 (2002)
51. Martel H, Shapiro P R *Mon. Not. R. Astron. Soc.* **297** 467 (1998)
52. Gnedin N Y, Kravtsov A V, Rudd D H *Astrophys. J. Suppl.* **194** 46 (2011)
53. Bertschinger E *Annu. Rev. Astron. Astrophys.* **36** 599 (1998)
54. Kuhlen M, Vogelsberger M, Angulo R *Phys. Dark Universe* **1** 50 (2012)
55. Borgani S, Kravtsov A *Adv. Sci. Lett.* **4** 204 (2011)
56. Kravtsov A V et al. *Astrophys. J.* **609** 35 (2004)
57. Kravtsov A V, Klypin A A *Astrophys. J.* **520** 437 (1999)
58. Sunyaev R A, Zeldovich Ya B *Astron. Astrophys.* **20** 189 (1972)
59. Klypin A A, Kates R E *Mon. Not. R. Astron. Soc.* **251** 41P (1991)
60. Cen R, Ostriker J P *Astrophys. J.* **514** 1 (1999)
61. Davé R et al. *Astrophys. J.* **552** 473 (2001)
62. Van Waerbeke L, Hinshaw G, Murray N *Phys. Rev. D* **89** 023508 (2014); arXiv:1310.5721
63. Sunyaev R A, Zeldovich Ya B *Comm. Astrophys. Space Phys.* **4** 173 (1972)
64. Sunyaev R A, Zel'dovich Ya B *Annu. Rev. Astron. Astrophys.* **18** 537 (1980)
65. White S D M, Rees M J *Mon. Not. R. Astron. Soc.* **183** 341 (1978)
66. Zeldovich Y B et al. *Sov. J. Nucl. Phys.* **31** 664 (1980); *Yad. Fiz.* **31** 1286 (1980)
67. Blumenthal G R et al. *Astrophys. J.* **301** 27 (1986)
68. Gnedin O Y et al. *Astrophys. J.* **616** 16 (2004)
69. Kazantzidis S et al. *Astrophys. J.* **611** L73 (2004)
70. Kravtsov A V, Borgani S *Annu. Rev. Astron. Astrophys.* **50** 353 (2012)
71. Vikhlinin A et al. *Astrophys. J.* **640** 691 (2006)
72. Carlstrom J E, Holder G P, Reese E D *Annu. Rev. Astron. Astrophys.* **40** 643 (2002)
73. Lyskova N et al. *Mon. Not. R. Astron. Soc.* **423** 1813 (2012)
74. Hoekstra H, arXiv:1312.5981
75. Allen S W, Evrard A E, Mantz A B *Annu. Rev. Astron. Astrophys.* **49** 409 (2011)
76. Press W H, Schechter P *Astrophys. J.* **187** 425 (1974)
77. Gunn J E, Gott J R (III) *Astrophys. J.* **176** 1 (1972)
78. Percival W J *Astron. Astrophys.* **443** 819 (2005)
79. Klypin A et al. *Astrophys. J.* **444** 1 (1995)
80. Gross M A K et al. *Mon. Not. R. Astron. Soc.* **301** 81 (1998)
81. Lee J, Shandarin S F *Astrophys. J.* **517** L5 (1999)
82. Sheth R K, Tormen G *Mon. Not. R. Astron. Soc.* **308** 119 (1999)
83. Jenkins A et al. *Mon. Not. R. Astron. Soc.* **321** 372 (2001)
84. Monaco P *Astrophys. J.* **447** 23 (1995)
85. Audit E, Teyssier R, Alimi J-M *Astron. Astrophys.* **325** 439 (1997)
86. Sheth R K, Mo H J, Tormen G *Mon. Not. R. Astron. Soc.* **323** 1 (2001)
87. Sheth R K, Tormen G *Mon. Not. R. Astron. Soc.* **329** 61 (2002)
88. Tinker J L et al. *Astrophys. J.* **724** 878 (2010)
89. Watson W A et al. *Mon. Not. R. Astron. Soc.* **433** 1230 (2013)
90. Warren M S, in *Proc. SC'13: Intern. Conf. for High Performance Computing, Networking, Storage and Analysis, November 17–21 2013* (New York: ACM, 2013) Article No. 72, DOI:10.1145/2503210.2503220; arXiv:1310.4502
91. Rudd D H, Zentner A R, Kravtsov A V *Astrophys. J.* **672** 19 (2008)
92. Cui W et al. *Mon. Not. R. Astron. Soc.* **423** 2279 (2012)
93. Martizzi D et al. *Mon. Not. R. Astron. Soc.*, submitted; arXiv:1307.6002
94. Desjacques V *Mon. Not. R. Astron. Soc.* **388** 638 (2008)
95. Maggiore M, Riotto A *Astrophys. J.* **717** 515 (2010)
96. de Simone A, Maggiore M, Riotto A *Mon. Not. R. Astron. Soc.* **412** 2587 (2011)
97. Ma C-P et al. *Mon. Not. R. Astron. Soc.* **411** 2644 (2011)
98. Corasaniti P S, Achitouv I *Phys. Rev. Lett.* **106** 241302 (2011)
99. Lim S, Lee J *JCAP* (01) 019 (2013)
100. Achitouv I et al. *Phys. Rev. Lett.* **111** 231303 (2013)
101. Tinker J et al. *Astrophys. J.* **688** 709 (2008)
102. Courtin J et al. *Mon. Not. R. Astron. Soc.* **410** 1911 (2011)
103. Hoekstra H *Mon. Not. R. Astron. Soc.* **379** 317 (2007)
104. Applegate D E et al. *Mon. Not. R. Astron. Soc.* **439** 48 (2014); arXiv:1208.0605
105. Rasia E, Tormen G, Moscardini L *Mon. Not. R. Astron. Soc.* **351** 237 (2004)
106. Nagai D, Vikhlinin A, Kravtsov A V *Astrophys. J.* **655** 98 (2007)
107. Piffaretti R, Valdarnini R *Astron. Astrophys.* **491** 71 (2008)
108. Lau E T, Kravtsov A V, Nagai D *Astrophys. J.* **705** 1129 (2009)
109. Nelson K et al. *Astrophys. J.* **751** 121 (2012)
110. Becker M R, Kravtsov A V *Astrophys. J.* **740** 25 (2011)
111. Kravtsov A V, Vikhlinin A, Nagai D *Astrophys. J.* **650** 128 (2006)
112. Pratt G W et al. *Astron. Astrophys.* **498** 361 (2009)
113. Motl P M et al. *Astrophys. J.* **623** L63 (2005)
114. Nagai D *Astrophys. J.* **650** 538 (2006)
115. Nagai D, Kravtsov A V, Vikhlinin A *Astrophys. J.* **668** 1 (2007)
116. Stanek R et al. *Astrophys. J.* **715** 1508 (2010)
117. Fabjan D et al. *Mon. Not. R. Astron. Soc.* **416** 801 (2011)
118. Riess A G et al. *Astron. J.* **116** 1009 (1998)
119. Perlmutter S et al. *Astrophys. J.* **517** 565 (1999)
120. Sunyaev R A, Zeldovich Ya B *Astrophys. Space Sci.* **7** 3 (1970)
121. Albrecht A et al., astro-ph/0609591
122. Fosalba P, Gaztañaga E, Castander F J *Astrophys. J.* **597** L89 (2003)
123. Guzzo L et al. *Nature* **451** 541 (2008)
124. Huterer D, Linder E V *Phys. Rev. D* **75** 023519 (2007)
125. Sunyaev R A, Zeldovich Y B *Comm. Astrophys. Space Phys.* **4** 173 (1972)
126. Sasaki S *Publ. Astron. Soc. Jpn.* **48** L119 (1996)
127. Pen U-L *New Astron.* **2** 309 (1997)
128. Oukbir J, Blanchard A *Astron. Astrophys.* **262** L21 (1992)
129. Borgani S, Kravtsov A *Adv. Sci. Lett.* **4** 204 (2011); arXiv:0906.4370
130. Rosati P, Borgani S, Norman C *Annu. Rev. Astron. Astrophys.* **40** 539 (2002)
131. Ebeling H et al. *Mon. Not. R. Astron. Soc.* **318** 333 (2000)
132. Böhringer H et al. *Astron. Astrophys.* **425** 367 (2004)
133. Ebeling H, Edge A C, Henry J P *Astrophys. J.* **553** 668 (2001)
134. Burenin R A et al. *Astrophys. J. Suppl.* **172** 561 (2007)
135. Williamson R et al. *Astrophys. J.* **738** 139 (2011)
136. Marriage T A et al. *Astrophys. J.* **737** 61 (2011); arXiv:1010.1065
137. Ade P A R et al. (Planck Collab.) *Astron. Astrophys.* **536** A8 (2011); arXiv:1101.2024
138. Vikhlinin A et al. *Astrophys. J.* **640** 691 (2006)
139. Sun M et al. *Astrophys. J.* **693** 1142 (2009)
140. Pratt G W et al. *Astron. Astrophys.* **461** 71 (2007)
141. Nagai D, Kravtsov A V, Vikhlinin A *Astrophys. J.* **668** 1 (2007)
142. Pratt G W et al. *Astron. Astrophys.* **511** A85 (2010); arXiv:0909.3776
143. Pierpaoli E et al. *Mon. Not. R. Astron. Soc.* **342** 163 (2003)
144. Henry J P et al. *Astrophys. J.* **691** 1307 (2009)
145. Rasia E et al. *Mon. Not. R. Astron. Soc.* **369** 2013 (2006)
146. Nagai D, Vikhlinin A, Kravtsov A V *Astrophys. J.* **655** 98 (2007)
147. Vikhlinin A et al. *Astrophys. J.* **692** 1060 (2009)
148. Rozo E et al. *Astrophys. J.* **708** 645 (2010); arXiv:0902.3702
149. Fu L et al. *Astron. Astrophys.* **479** 9 (2008)
150. Bonamente M et al. *Astrophys. J.* **647** 25 (2006)
151. White S D M et al. *Nature* **366** 429 (1993)
152. Gonzalez A H, Zaritsky D, Zabludoff A I *Astrophys. J.* **666** 147 (2007)
153. Allen S W et al. *Mon. Not. R. Astron. Soc.* **383** 879 (2008)
154. Linder E V, Jenkins A *Mon. Not. R. Astron. Soc.* **346** 573 (2003)
155. Carilli C L, Taylor G B *Annu. Rev. Astron. Astrophys.* **40** 319 (2002)
156. Bonafede A et al. *Astron. Astrophys.* **513** A30 (2010)
157. Feretti L et al. *Astron. Astrophys. Rev.* **20** 54 (2012)
158. ZuHone J A et al. *Astrophys. J.* **762** 78 (2013)
159. Churazov E et al. *Mon. Not. R. Astron. Soc.* **388** 1062 (2008)
160. Sunyaev R A *Astron. Astrophys.* **12** 190 (1971)
161. Bahcall J N, Sarazin C L *Astrophys. J.* **213** L99 (1977)
162. Markevitch M et al. *Astrophys. J.* **567** L27 (2002)
163. Markevitch M et al. *Astrophys. J.* **627** 733 (2005)
164. Russell H R et al. *Mon. Not. R. Astron. Soc.* **406** 1721 (2010)

165. Russell H R et al. *Mon. Not. R. Astron. Soc.* **423** 236 (2012)
166. Macario G et al. *Astrophys. J.* **728** 82 (2011)
167. Akamatsu H et al. *Publ. Astron. Soc. Jpn.* **64** 49 (2012)
168. Akamatsu H et al. *Publ. Astron. Soc. Jpn.* **64** 67 (2012)
169. Akamatsu H, Kawahara H *Publ. Astron. Soc. Jpn.* **65** 16 (2013)
170. Giacintucci S et al. *Astron. Astrophys.* **486** 347 (2008)
171. Bourdin H et al. *Astrophys. J.* **764** 82 (2013)
172. Ade P A R et al. (Planck Collab.) *Astron. Astrophys.* **554** A140 (2013)
173. Markevitch M, in *Proc. of the X-Ray Universe 2005. 26–30 September 2005, Madrid, Spain* (ESA Special Publ., Vol. 604, Ed. A Wilson) (Noordwijk: ESA Publ. Division, ESTEC, 2006) p. 723
174. Owers M S et al. *Astrophys. J.* **704** 1349 (2009)
175. Markevitch M, in preparation
176. Springel V, Farrar G R *Mon. Not. R. Astron. Soc.* **380** 911 (2007)
177. Clowe D, Gonzalez A, Markevitch M *Astrophys. J.* **604** 596 (2004)
178. Clowe D et al. *Astrophys. J.* **648** L109 (2006)
179. Markevitch M, Vikhlinin A *Phys. Rep.* **443** 1 (2007)
180. Markevitch M et al. *Astrophys. J.* **606** 819 (2004)
181. Barrena R et al. *Astron. Astrophys.* **386** 816 (2002)
182. Milgrom M *Astrophys. J.* **270** 365 (1983)
183. Brownstein J R, Moffat J W *Mon. Not. R. Astron. Soc.* **367** 527 (2006)
184. Bradač M et al. *Astrophys. J.* **687** 959 (2008)
185. Ragozzine B et al. *Astrophys. J.* **744** 94 (2012)
186. Clowe D et al. *Astrophys. J.* **758** 128 (2012)
187. Spergel D N, Steinhardt P J *Phys. Rev. Lett.* **84** 3760 (2000)
188. Randall S W et al. *Astrophys. J.* **679** 1173 (2008)
189. Merten J et al. *Mon. Not. R. Astron. Soc.* **417** 333 (2011)
190. Mahdavi A et al. *Astrophys. J.* **668** 806 (2007)
191. Miralda-Escudé J *Astrophys. J.* **564** 60 (2002)
192. Spitzer L *Physics of Fully Ionized Gases* (New York: Interscience Publ., 1962)
193. Zel'dovich Ya B, Raizer Yu P *Physics of Shock Waves and High-Temperature Hydrodynamic Phenomena* (New York: Academic Press, 1966, 1967); Translated from Russian: *Fizika Udarnykh Voln i Vysokotemperaturnykh Gidrodinamicheskikh Yavlenii* (Moscow: Fizmatgiz, 1963)
194. Vikhlinin A, Markevitch M, Murray S S *Astrophys. J.* **551** 160 (2001)
195. Lyutikov M *Mon. Not. R. Astron. Soc.* **373** 73 (2006)
196. Shafranov V D *Sov. Phys. JETP* **5** 1183 (1957); *Zh. Eksp. Teor. Fiz.* **32** 1453 (1957)
197. Wik D R et al. *Astrophys. J.* **696** 1700 (2009)
198. Wik D R et al. *Astrophys. J.*, submitted (2014); arXiv:1403.2722
199. Ackermann M et al. (The Fermi-LAT Collab.) *Science* **339** 807 (2013); arXiv:1302.3307
200. Brunetti G, Jones T W, arXiv:1401.7519
201. Cassano R, Brunetti G, Venturi T *J. Astrophys. Astron.* **32** 519 (2011)
202. Blandford R, Eichler D *Phys. Rep.* **154** 1 (1987)
203. van Weeren R J et al. *Science* **330** 347 (2010)
204. Ogrean G A et al. *Mon. Not. R. Astron. Soc.* **429** 2617 (2013)
205. Brunetti G et al. *Nature* **455** 944 (2008)
206. Giacintucci S et al., in preparation
207. Brown S, Rudnick L *Mon. Not. R. Astron. Soc.* **412** 2 (2011)
208. Ogrean G A et al. *Mon. Not. R. Astron. Soc.* **433** 812 (2013)
209. Kang H, Jones T W *J. Korean Astron. Soc.* **35** 159 (2002)
210. Sarazin C L *Astrophys. J.* **520** 529 (1999)
211. Kang H, Jones T W *Astrophys. J.* **620** 44 (2005)
212. Pinzke A, Oh S P, Pfrommer C *Mon. Not. R. Astron. Soc.* **435** 1061 (2013)
213. Brunetti G, Lazarian A *Mon. Not. R. Astron. Soc.* **378** 245 (2007)
214. Shimwell T W et al. *Mon. Not. R. Astron. Soc.*, submitted (2014); arXiv:1403.2393
215. McNamara B R, Nulsen P E J *Annu. Rev. Astron. Astrophys.* **45** 117 (2007)
216. Fabian A C *Annu. Rev. Astron. Astrophys.* **50** 455 (2012)
217. Lea S M *Astrophys. J.* **203** 569 (1976)
218. Cowie L L, Binney J *Astrophys. J.* **215** 723 (1977)
219. Fabian A C, Nulsen P E J *Mon. Not. R. Astron. Soc.* **180** 479 (1977)
220. Fabian A C *Annu. Rev. Astron. Astrophys.* **32** 277 (1994)
221. Peterson J R, Fabian A C *Phys. Rep.* **427** 1 (2006)
222. Pedlar A et al. *Mon. Not. R. Astron. Soc.* **246** 477 (1990)
223. Tabor G, Binney J *Mon. Not. R. Astron. Soc.* **263** 323 (1993)
224. Binney J, Tabor G *Mon. Not. R. Astron. Soc.* **276** 663 (1995)
225. Böhringer H et al. *Mon. Not. R. Astron. Soc.* **264** L25 (1993)
226. Böhringer H et al. *Mon. Not. R. Astron. Soc.* **274** L67 (1995)
227. Churazov E et al. *Astron. Astrophys.* **356** 788 (2000)
228. Churazov E et al. *Astrophys. J.* **554** 261 (2001)
229. McNamara B R et al. *Astrophys. J.* **534** L135 (2000)
230. Forman W et al. *Astrophys. J.* **635** 894 (2005)
231. Dunn R J H, Fabian A C *Mon. Not. R. Astron. Soc.* **373** 959 (2006)
232. Rafferty D A et al. *Astrophys. J.* **652** 216 (2006)
233. Hlavacek-Larrondo J et al. *Mon. Not. R. Astron. Soc.* **421** 1360 (2012)
234. Bîrzan L et al. *Mon. Not. R. Astron. Soc.* **427** 3468 (2012)
235. Hines D C, Eilek J A, Owen F N *Astrophys. J.* **347** 713 (1989)
236. Owen F N, Eilek J A, Kassim N E *Astrophys. J.* **543** 611 (2000)
237. Forman W et al. *Astrophys. J.* **665** 1057 (2007)
238. Fabian A C et al. *Mon. Not. R. Astron. Soc.* **344** L48 (2003)
239. Werner N et al. *Mon. Not. R. Astron. Soc.* **407** 2063 (2010)
240. Churazov E et al. *Mon. Not. R. Astron. Soc.* **332** 729 (2002)
241. Fabian A C et al. *Mon. Not. R. Astron. Soc.* **366** 417 (2006)
242. Randall S W et al. *Astrophys. J.* **726** 86 (2011)
243. McNamara B R et al. *Nature* **433** 45 (2005)
244. Böhringer H et al. *Astron. Astrophys.* **382** 804 (2002)
245. Bondi H *Mon. Not. R. Astron. Soc.* **112** 195 (1952)
246. Allen S W et al. *Mon. Not. R. Astron. Soc.* **372** 21 (2006)
247. Pizzolato F, Soker N *Astrophys. J.* **632** 821 (2005)
248. Gaspari M, Ruszkowski M, Sharma P *Astrophys. J.* **746** 94 (2012)
249. Churazov E et al. *Mon. Not. R. Astron. Soc.* **363** L91 (2005)
250. Sazonov S Yu, Ostriker J P, Sunyaev R A *Mon. Not. R. Astron. Soc.* **347** 144 (2004)
251. Sazonov S Yu et al. *Mon. Not. R. Astron. Soc.* **358** 168 (2005)
252. Ichimaru S *Astrophys. J.* **214** 840 (1977)
253. Rees M J et al. *Nature* **295** 17 (1982)
254. Narayan R, Yi I *Astrophys. J.* **428** L13 (1994)
255. Gallo E, Fender R P, Pooley G G *Mon. Not. R. Astron. Soc.* **344** 60 (2003)
256. Croton D J et al. *Mon. Not. R. Astron. Soc.* **365** 11 (2006)
257. Bower R G et al. *Mon. Not. R. Astron. Soc.* **370** 645 (2006)